Nanoscale
Advances

ROYAL SOCIETY
OF CHEMISTRY

MINIREVIEW

View Article Online
View Journal | View Issue

Cite this: *Nanoscale Adv.*, 2023, **5**, 3589

Received 3rd April 2023
Accepted 25th May 2023

DOI: 10.1039/d3na00213f

rsc.li/nanoscale-advances

# Recent strategies for constructing hierarchical multicomponent nanoparticles/metal–organic framework hybrids and their applications

Ngoc Minh Tran, Anh Ngoc Nguyen, Jungeun Bae, Jinhee Kim, Dahae Kim and Hyojong Yoo *

Hybrid nanoparticles with unique tailored morphologies and compositions can be utilized for numerous applications owing to their combination of inherent properties as well as the structural and supportive functions of each component. Controlled encapsulation of nanoparticles within nanospaces (NPNSs) of metal–organic frameworks (MOFs) (denoted as NPNS@MOF) can generate a large number of hybrid nanomaterials, facilitating superior activity in targeted applications. In this review, recent strategies for the fabrication of NPNS@MOFs with a hierarchical architecture, tailorability, unique intrinsic properties, and superior catalytic performance are summarized. In addition, the latest and most important examples in this sector are emphasized since they are more conducive to the practical applicability of NPNS@MOF nanohybrids.

## 1. Introduction

Metal–organic frameworks (MOFs), new types of porous hybrid materials generated by the self-assembly of metal ions and/or metal clusters and multitopic organic ligands, are emerging as versatile precursors or templates for constructing numerous advanced functional nanomaterials.[1–3] Owing to their unique characteristics such as a high degree of porosity, well-defined pore size, and structural tailorability, MOFs have been utilized for diverse applications.[4–6] Particularly, the main advantages of MOFs in catalytic processes and related applications[7–9] are summarized as follows: (i) the well-designed framework contains different types of active moieties, including metal ions and/or metal clusters combined with functional groups of the organic linkers;[10,11] (ii) the uniform dispersion and high density of active sites can significantly improve the catalytic activity;[12,13] (iii) the high degree of porous structures allows each active species to be exposed, while the channel system provides a favorable environment for the diffusion and transportation of both reactants and products;[14–16] (iv) the suitable hydrophilic and hydrophobic properties of MOFs can control the interactions of reactants with the framework to enhance the catalytic performances, including efficiency and selectivity.[17,18] With all the above advantages, the role of MOFs in the development of advanced nanomaterials is immensely crucial.[19,20]

Hybrid nanostructures with unique tailored morphologies and compositions can be utilized for diversified and targeted applications,[21–23] owing to the inherent properties as well as the synergistic effects of each component.[24–26] Nanoparticles in this study refer to particles with at least one nanoscale dimension, exhibiting distinctive physical and chemical properties that differ from those of their bulk counterparts.[27–29] The controllable encapsulation of nanoparticles, such as metal and/or metal oxide nanoparticles into MOFs, can generate numerous hybrid nanomaterials.[30–32] More importantly, by manipulating the sizes, shapes, and compositions of the nanoparticles within nanospaces (denoted as NPNSs) of MOFs[33–35] (NPNS@MOF), the resulting NPNS@MOF products show superior activity in targeted applications. It should be noted that the term NPNS@MOF nanohybrids in this review refers to nanospace-confinement structures containing nanoparticles (*e.g.*, metals, metal oxides, or inorganic-based compounds) dispersed within the nanospace generated by the MOF shell or between the core and the MOF shell, in which the nanoparticles can move freely. The importance of NPNS@MOF hybrid nanomaterials obtained through nanospace engineering, particularly with hollow structures, is due to the following advantages: (i) the well-defined and inherent structural features of individual components, including the exposed crystal facet, diameter, and uniformity of NPNSs, and the structural tailorability, micropores, and channel system of MOFs, can be simultaneously controlled; (ii) the abundant porosity and high surface area of MOFs, which are highly desirable for hosting guest species, can maximize the integration and controllable growth of NPNSs with size-, shape-, and morphological-dependent properties; (iii) the catalytically active sites can be protected *via* the stabilization of NPNSs against agglomeration and growth, poisoning, and/or calcination, and solution-based chemical etching, enhancing the performance and stability of active

---

*Department of Materials Science and Chemical Engineering, Hanyang University, Ansan, Gyeonggi-do, 15588, Republic of Korea. E-mail: hjhaha73@hanyang.ac.kr*

components; (iv) the pore size and channel architecture of the MOF component are precisely controlled, and therefore, NPNS@MOF nanohybrids can provide various efficient diffusion pathways and improve the selectivity of catalytic processes through molecular sieving capability; (v) the modifiability and tunability of the MOF shell have benefits in regulating the microenvironment around the active sites of NPNSs and their interactions with substrates, thereby improving catalytic selectivity; (vi) the nanospace generated between the NPNS and the MOF can facilitate not only the diffusion of substrates to the catalytically active species but also the release of products from the active surface, as well as offering sufficient spaces for the nanoparticles to access the substrates.

Herein, recent important strategies for the preparation of NPNS@MOF hybrid nanomaterials are summarized, and representative examples in this area are emphasized since they are more conducive to the practical applications of NPNS@MOFs. Altogether, this review provides a preliminary database for the fabrication of NPNS@MOFs and their applications. It is expected to direct the design of NPNS@MOF by providing details on synthetic strategies, structural features, and related applications, thereby potentially paving the way for the development of advanced multi-functional materials in relevant disciplines.

## 2. Recent strategies for the preparation of NPNS@MOF hybrid nanomaterials

In this section, we summarize the recently developed synthetic strategies that integrate nanoparticles within the nanospace of MOFs to generate NPNS@MOF hybrid nanomaterials with hollow architectures.[36] The synthesis and applications of five categories of NPNS@MOF hybrid nanomaterials are discussed in sequence, including metal nanoparticles encapsulated in yolk–shell, multiyolk–shell, yolk–multishell, rattle-type, and dot-in-shell NPNS@MOF nanohybrids (Fig. 1 and Scheme 1).[37] Notably, examples of nanoparticle-integrated MOFs and/or other supports without possessing hollow architectures (*e.g.*, core–shell and composites) and nanoparticle-integrated MOF-derived hollow nanohybrids, which have been well-reviewed elsewhere,[38–45] are outside the scope of this review.

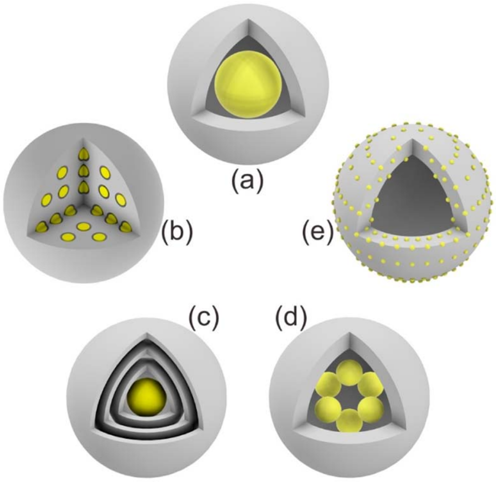

Fig. 1 Schematic illustration of different NPNS@MOF hybrid nanomaterials: (a) yolk–shell, (b) multiyolk–shell, (c) yolk–multishell, (d) rattle-type, and (e) dot-in-shell NPNS@MOF nanoarchitectures.

### 2.1. Yolk–shell NPNS@MOF nanohybrids

Currently, the template approach is one of the most straightforward and useful routes for the fabrication of yolk–shell NPNS@MOF nanohybrids. The shape, size, and nanospace within the structure of the obtained nanohybrids can be precisely controlled using the as-synthesized templates. The yolk–shell nanoarchitecture can be obtained by introducing nanoparticles for the subsequent MOF construction, involving a metal oxide (*e.g.*, $Cu_2O$) as an intermediate and nanospace creator, leading to the generation of core@nanospace@shell systems.[46] The very early example of yolk–shell Pd-NPNS@MOF nanohybrids was reported by Tsung *et al.*[47] In the synthesis, the as-prepared Pd nanoparticles were coated with a $Cu_2O$ layer as a sacrificial template to construct an outer shell ZIF-8 (Fig. 2).

The $Cu_2O$ layer was then simultaneously etched off by the protons formed during the generation of ZIF-8. The trace amount of $Cu_2O$ residue was removed by reacting with 3% $NH_4OH$ in methanolic solution. Using this strategy, a series of NPNS@ZIF-8 with yolk–shell architectures were fabricated. Importantly, the morphology and size of the as-prepared Pd nanoparticles were maintained during the loading of ZIF-8. Sindoro *et al.* investigated the evolution of core–shell NPNS@ZIF-8 nanoparticles into yolk–shell nanosystems along with the recrystallization of ZIF-8 (Fig. 3).[48] The formation pathway of yolk–shell NPNS@ZIF-8 could be monitored from TEM images (Fig. 3b–d). The ZIF-8 shell nucleated directly on the surface of the hematite core, generating a continuous crystalline coverage. The nanospaces between the core and shell were formed over time owing to the polycrystallinity of the ZIF-8 shell. The average shell thickness was preserved after encapsulation to yield the final yolk–shell architecture. The TEM images shown in Fig. 3e confirm that the yolk–shell NPNS@ZIF-8 nanostructures could be observed using the cores with different shapes through geometrical frustration. Another strategy to prepare yolk–shell NPNS@ZIF-8 nanostructures was reported by Li *et al.* (Fig. 4).[49] By using the self-template approach, the yolk–shell Pd-NPNS@ZIF-8 nanoparticle was successfully synthesized by reactions of the as-prepared core–shell Pd@ZnO nanostructure with 2-methylimidazole in methanolic solution. In this encapsulation strategy, ZnO served as a dual-functional species, as the self-template and $Zn^{2+}$ source for the construction of the ZIF-8 shell. Yang *et al.* demonstrated the fabrication of yolk–shell Pd-NPNS@ZIF-8 nanosystems *via* the emulsion-based interfacial process.[50] The abovementioned examples suggest that the self-sacrificial template route looks capable and sustainable for the synthesis of yolk–shell NPNS@MOF nanoparticles.

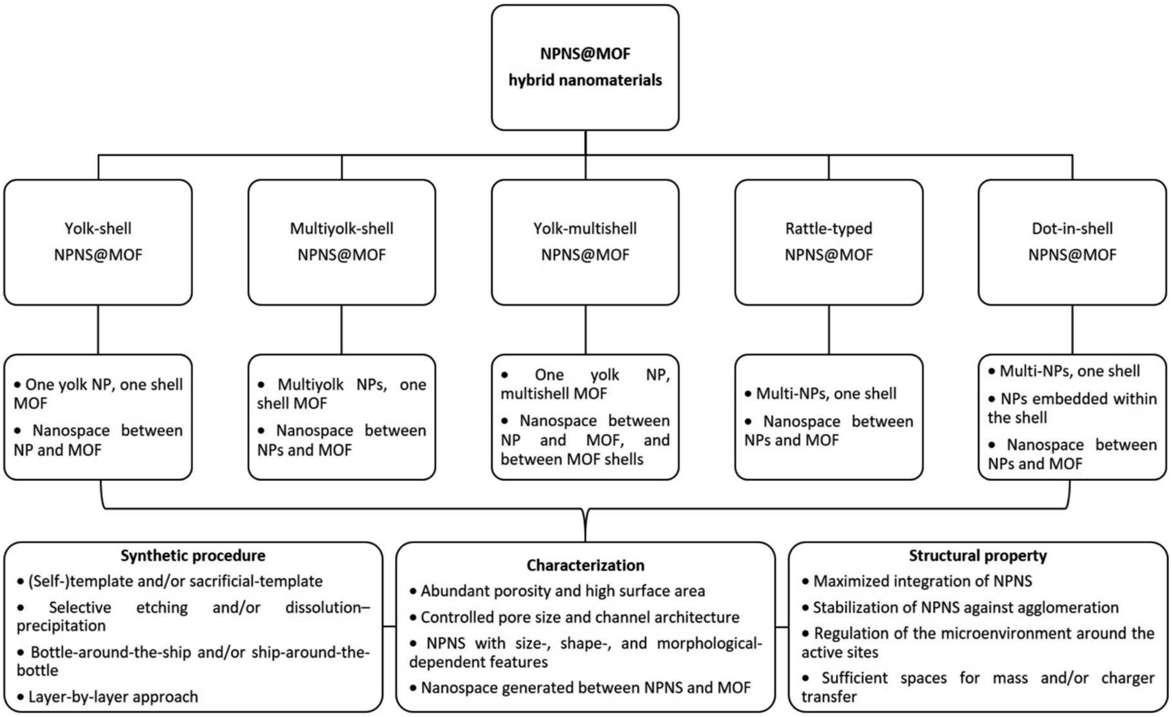

Scheme 1 Summary of the classification and characterization of NPNS@MOF hybrid nanomaterials.

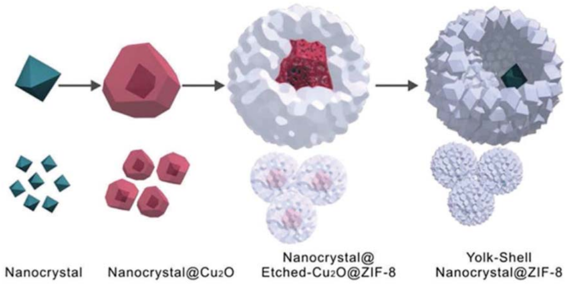

Fig. 2 Schematic growth procedure for the yolk–shell NPNS@ZIF-8 nanostructure (Copyright 2012, American Chemical Society).[47]

During the process, the initial shells not only can serve as the template for the construction of new shells but are also subsequently dissolved to provide the metal ion source for the new shells, requiring no additional removal of the template.

Yolk–shell NPNS@MOF nanohybrids have also been prepared without employing sacrificial templates.[51–53] For example, rationally designed and fabricated remote-controllable and stimuli-responsive yolk–shell Au-NPNS@ZIF-8 nanosystems for drug carriers were demonstrated.[54] Gold star nanoparticles were selected as the second-near-infrared photothermal conversion agents due to their strong absorption capacity in the second-near-infrared region. The synthetic procedure is illustrated in Fig. 5. In this process, star-shaped Au nanoparticles were first synthesized by reduction of the gold precursor using a mixture of polyvinylpyrrolidone and DMF without additional reducing agents. Next, ZIF-8 was loaded onto

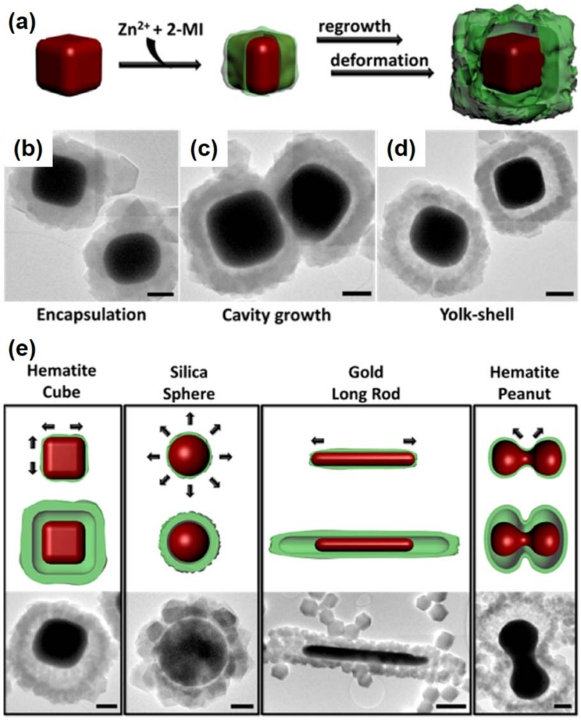

Fig. 3 (a) Schematic concept of yolk–shell NPNS@ZIF-8 generation with a cubic hematite crystal as the core and ZIF-8 as the shell, (b–d) TEM images of the growth pathway, and (e) schematic illustrations of the dominant deformation directions during shell growth (top) and yolk–shell architecture generation (middle), accompanied by TEM images (bottom). Scale bars: 500 nm (Copyright 2014, American Chemical Society).[48]

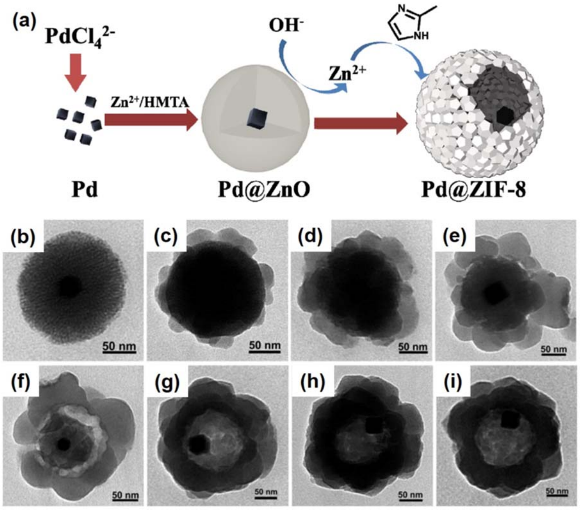

Fig. 4 (a) Schematic illustration of the fabrication of yolk–shell Pd-NPNS@ZIF-8 nanoparticles *via* the self-template approach, (b) TEM image of core–shell Pd@ZnO nanoparticles, and (c–i) time-resolved TEM images illustrating the structural evolution of yolk–shell Pd-NPNS@ZIF-8 nanoparticles as a function of reaction time: (c) 5 min, (d) 10 min, (e) 20 min, (f) 30 min, (g) 60 min, (h) 120 min, and (i) 240 min (Copyright 2016, Royal Society of Chemistry).[49]

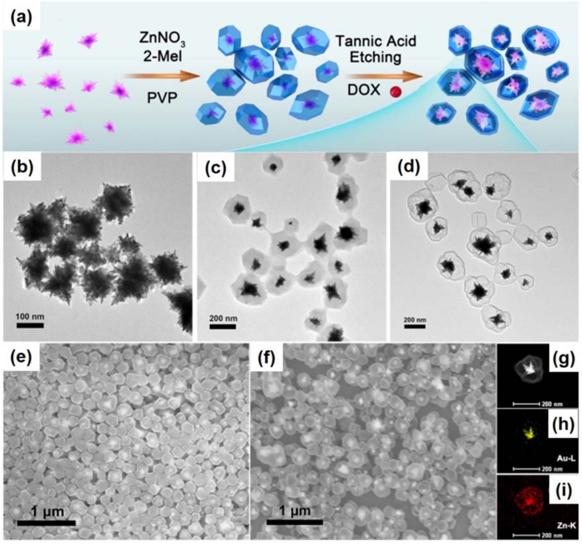

Fig. 5 (a) Schematic illustration for the fabrication of yolk–shell Au-NPNS@ZIF-8 nanosystems; (b–d) TEM images of (b) Au star nanoparticles, (c) Au@ZIF-8, and (d) yolk–shell Au-NPNS@ZIF-8 nanostructures; (e and f) SEM images of (e) Au@ZIF-8 and (f) yolk–shell Au-NPNS@ZIF-8 nanostructures; (g–i) TEM image and EDS elemental mapping of one single Au-NPNS@ZIF-8 nanoparticle (Copyright 2019, American Chemical Society).[54]

the surface of the Au stars. Yolk–shell Au-NPNS@ZIF-8 nanostructures were then prepared *via* selective etching using tannic acid. The nanospace formed between the yolk and shell acted as a storage vessel for chemotherapeutic drug delivery. This study is a good example of multi-functional yolk–shell NPNS@ZIF-8 nanohybrids applied for theranostic research. The abovementioned examples indicated that the surfactant, polyvinylpyrrolidone (PVP), plays a vital role in the hierarchical construction and morphology regulation of NPNS@MOF nanohybrids.[55] Particularly, PVP can simultaneously serve as a dispersing agent, structure-directing agent, and capping agent; therefore, PVP can control the growth of NPNS.

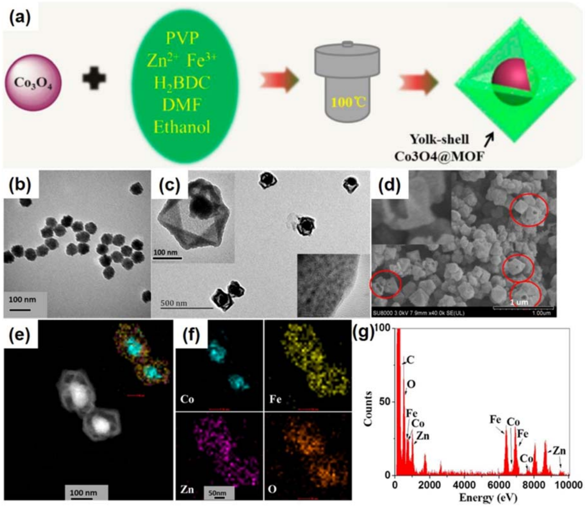

Fig. 6 (a) Synthetic strategy for yolk–shell $Co_3O_4$-NPNS@MOF nanostructures; TEM images of (b) $Co_3O_4$ nanoparticles and (c) yolk–shell $Co_3O_4$-NPNS@MOF nanostructures; (d) SEM image, (e) HAADF-STEM image, (f) elemental mapping, and (g) EDX spectra of yolk–shell $Co_3O_4$-NPNS@MOF nanostructures. The insets in (c) show the closer TEM observation (Copyright 2015, American Chemical Society).[56]

Metallic nanoparticles can be used as nanoparticle species and metal oxides can be employed for the preparation of NPNS@MOF nanohybrids. However, a few studies have focused on the synthesis of metal oxide-NPNS@MOF nanosystems even though these materials are believed to extend the manipulation of MOFs for efficient catalysis, as well as utilizing magnetically induced heating for controllable drug delivery and release. For instance, Zeng *et al.* investigated the encapsulation of $Co_3O_4$ in a suitable hollow nanoarchitecture, yielding typical yolk–shell $Co_3O_4$-NPNS@MOF nanostructures (Fig. 6).[56] Importantly, the high degree of porosity of the MOF shell in the hollow nanoarchitecture can impede the aggregation of the $Co_3O_4$ moieties. Moreover, under a harsh external environment, the porous MOF prevents the encapsulated catalyst from being influenced without affecting the diffusion of both the reactants and products. Simultaneously, the exposed $Co_3O_4$ catalytically active sites are maintained and accessible to reactants in the interior nanospace of the $Co_3O_4$-NPNS@MOF nanoreactor, offering a microenvironment for the oxidization of $SO_4^{\bullet -}$.[57]

### 2.2. Multiyolk–shell NPNS@MOF nanohybrids

Multiyolk–shell NPNS@MOF nanoarchitectures, which contain both a multi-metal core and nanospaces within a single-shell MOF, have also received considerable attention because of their complex and hierarchical nanostructures. For

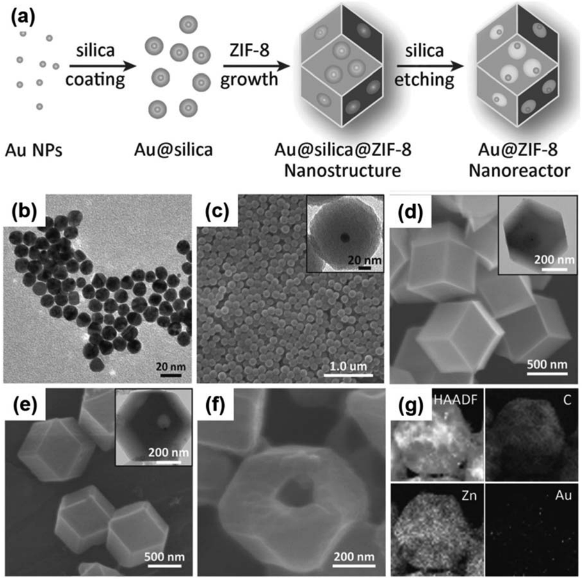

Fig. 7 (a) Schematic illustration of the fabrication of multiyolk–shell Au-NPNS@ZIF-8 nanohybrids; (b) TEM image of Au nanoparticles; (c–f) SEM images of (c) core–shell Au@silica nanoparticles, (d) core–shell–shell Au@silica@ZIF-8 nanoparticles, (e) yolk–shell Au-NPNS@ZIF-8 nanohybrids, and (f) cracked yolk–shell Au-NPNS@ZIF-8 nanostructures; the insets in (c–e) show the corresponding TEM images; (g) HAADF-STEM and EDX elemental mapping images of a multiyolk–shell Au-NPNS@ZIF-8 nanohybrid (Copyright 2016, Wiley-VCH).[58]

example, a sacrificial-template strategy was used to synthesize multiyolk–shell Au-NPNS@ZIF-8 nanohybrids composed of a single-crystal ZIF-8 shell with introduced macropores, each of which contained multiple Au nanoparticles (Fig. 7).[58] To achieve the multiyolk–shell Au-NPNS@ZIF-8 nanoarchitecture, a multi-step synthetic procedure was employed, including the first growth of core–shell Au@silica nanoparticles, followed by encapsulation of the obtained product in a single crystal ZIF-8 shell, and then etching of silica layers, in which the silica served as a sacrificial template, with an aqueous NaOH solution to generate the final nanohybrids. Unlike yolk–shell NPNS@MOF nanohybrids, which include a one-yolk moiety in the structure, the multiyolk–shell Au-NPNS@ZIF-8 nanohybrids contain up to 15 yolk units in each shell MOF. The quantity of yolk moieties per ZIF-8 shell can be readily controlled by the volume of the Au@silica nanoparticle solution employed for the preparation of core–shell–shell Au@silica@ZIF-8 nanosystems. The multiyolk–shell Au-NPNS@ZIF-8 nanoreactors not only increased the accessibility of Au nanoparticles to reactants but also enhanced the mass transfer kinetics of both substrates and products through their molecular sieving capability.

Another exciting example of the preparation of multiyolk–shell NPNS@MOF nanohybrids was demonstrated using a similar strategy to the aforementioned through the sacrificial-template method (Fig. 8).[59] Multiyolk–shell $Cu_2O$-NPNS@ZIF-8 was hierarchically fabricated by a four-step synthetic procedure. First, uniform $Cu_2O$ nanocubes were prepared by an ultrasound-assisted method. It should be emphasized that $Cu_2O$ shows high activity and diverse applications; however, its intrinsic poor stability is the main drawback, especially in solution. Next, the surface of $Cu_2O$ nanocubes was protected by a layer of the $SiO_2$ shell using tetraethoxysilane as the silica source. In this step, an aqueous NaOH solution was employed instead of an ammonia solution to catalyze the hydrolysis of silica because the unstable $Cu_2O$ nanocubes could be etched by ammonia solution. The obtained core–shell $Cu_2O@SiO_2$ nanostructures were then integrated into ZIF-8 nanocrystals through the "bottle around the ship" approach. Finally, the $SiO_2$ layer in the core-shell-shell $Cu_2O@SiO_2$@ZIF-8 nanoparticle was selectively etched with an aqueous NaOH solution to afford multiyolk–shell $Cu_2O$-NPNS@ZIF-8 nanohybrids with an average nanospace size of approximately 40 nm, generated between the $Cu_2O$ nanocube and ZIF-8 shell. A similar strategy has also been applied to synthesize multiyolk–shell NPNS@metal oxide nanoparticles.[40] However, it is believed that this is the first example of a multiyolk–shell NPNS@MOF nanosystem with metastable nanoparticle integration.

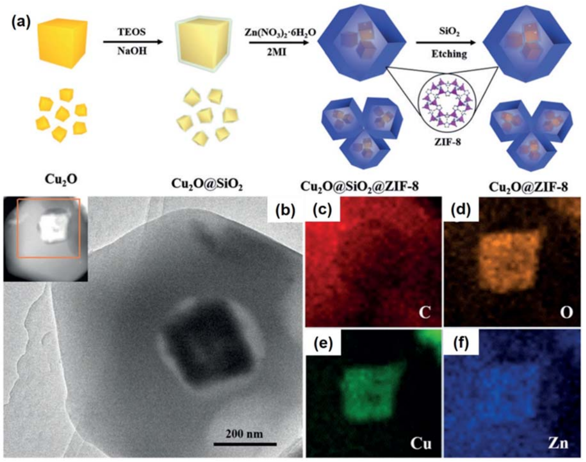

Fig. 8 (a) Schematic illustration for the preparation of the multiyolk–shell Au-NPNS@ZIF-8 nanoreactors; (b) TEM image and the HAADF-STEM image from (c); (c–f) elemental mapping of (c) carbon (in red), (d) oxygen (in orange), (e) copper (in green), and (f) zinc (in blue) (Copyright 2018, Wiley-VCH).[59]

Compared to other hybrid nanocatalysts (*e.g.*, zeolites and core–shell architectures), multiyolk–shell NPNS@MOFs exhibit some benefits. The diffusion length of the substrates can be effectively shortened by the thin wall of the shell, ensuring fast diffusion for both reactants and products, while retaining the protective functions and molecular sieving properties. Moreover, the large nanospace generated between the yolks and shell guarantees full preservation of the catalytically active sites on the surfaces of the nanohybrids, leading to maximum catalytic activity. Recently, Luo *et al.* reported a new strategy (oxidative linker cleaving) to construct multiyolk–shell NPNS@MOF nanohybrids (Fig. 9).[60] In the synthesis, 2,5-dihydroxyterephthalic acid was used as a sacrificial organic linker, which can generate small molecular fragments through selective cleavage by the oxidative ring-opening process. By controlling the

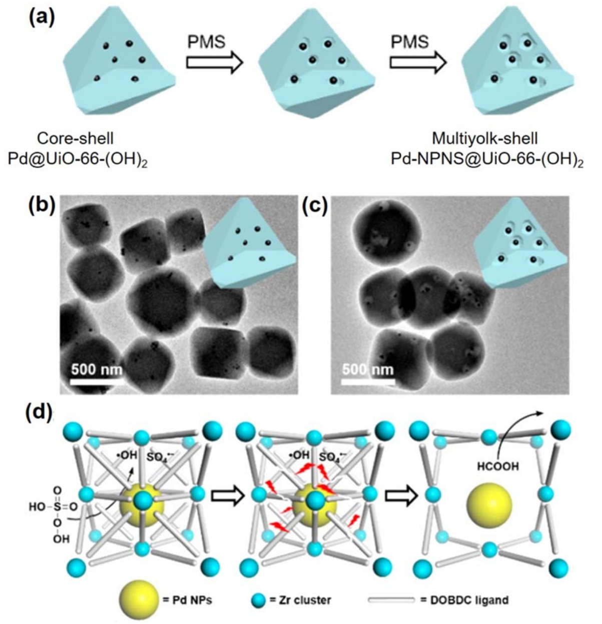

Fig. 9 (a) Schematic illustration for the localized oxidative linker cleaving process; (b and c) TEM images of (b) core–shell Pd@UiO-66-$(OH)_2$ and (c) multiyolk–shell NPNS@MOF nanostructures; (d) schematic illustration of the oxidative linker cleaving process catalyzed by Pd nanoparticles in core–shell Pd@UiO-66-$(OH)_2$ nanoparticles (abbreviations: PMS = peroxymonosulfate; DOBDC = 2,5-dihydroxyterephthalic acid) (Copyright 2019, American Chemical Society).[60]

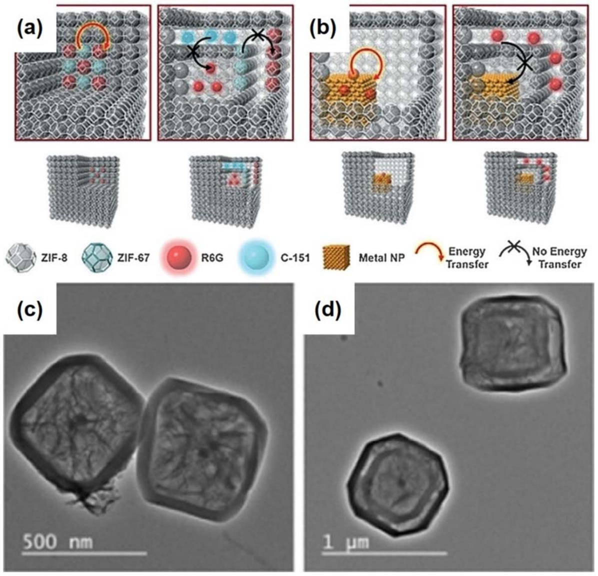

Fig. 10 (a and b) Models of yolk–multishell NPNS@ZIFs and the guest-to-host and guest-to-guest energy transfer: (a) energy transfer between guest C-151 and guest R6G (left) and prohibited energy transfer between guests (right); (b) energy transfer between guest Pd nanoparticles and guest R6G (left) and prohibited energy transfer (right). (c) Hollow R6G&Pd@ZIF-8 and (d) yolk–multishell Pd-NPNS@ZIF-8@R6G@ZIF-8 nanohybrids (abbreviations: C-151 = 7-amino-4-(trifluoromethyl)coumarin; R6G = rhodamine 6G) (Copyright 2018, Wiley-VCH).[61]

formation of oxidative species, UiO-66-$(OH)_2$ can be directionally engraved from outside to inside or reversibly, generating hollow UiO-66-$(OH)_2$ nanostructures. Interestingly, by employing the preformed Pd@UiO-66-$(OH)_2$ nanoparticles, the oxidative linker cleaving process could initially occur and localize around the Pd moiety, resulting in the formation of multiyolk–shell Pd-NPNS@UiO-66-$(OH)_2$ nanostructures.

### 2.3. Yolk–multishell NPNS@MOF nanohybrids

In addition to using single-phase MOFs for encapsulating nanoparticles to construct the aforementioned NPNS@MOF nanohybrids, multiple-phase MOFs with hierarchical architectures could be employed as host templates to encapsulate nanoparticles to achieve yolk–multishell NPNS@MOF nanohybrids. This strategy is inspired by biological systems, in which intricate functions often rely on the precise positions of multiple species in the multi-shelled architectures. Interactions between the components of biological systems are well-regulated. For example, mitochondria, one of the main regulators of cellular functions, have a multi-shelled hollow structure, in which the functional moieties with different roles are wandered in the intermembrane space or integrated into the membrane shells. To investigate this strategy, Liu *et al.* introduced Pd nanoparticles as the heterogeneous nanoparticles, as well as rhodamine 6G and 7-amino-4-(trifluoromethyl)coumarin as the molecular nanoparticles into the multi-shelled hollow ZIF-8 to afford a series of yolk–multishell NPNS@ZIFs nanohybrids (Fig. 10).[61] During this process, the nanoparticles were first encapsulated within different layers of the multi-layered ZIF nanocrystal *via* epitaxial layer-by-layer growth reactions. The multi-layered ZIFs, including ZIF-8 and ZIF-67, exhibited a well-defined onion configuration since ZIF-8 and ZIF-67 possess the same topology but different metal nodes, *i.e.*, Zn and Co, respectively. Next, the ZIF-67 parts were dissociated to generate the nanospace layers between the ZIF-8 counterparts. Therefore, the nanoparticles initially embedded in ZIF-8 layers were still embedded in the ZIF-8 shells, while the entities initially loaded in the ZIF-67 layers were released and encapsulated in the nanospace between ZIF-8 shells. Finally, the yolk–multishell NPNS@ZIF nanohybrids were obtained. By precisely embedding the nanoparticles within the ZIF shells or encapsulating them in the nanospaces between the ZIF shells, the energy transfer interactions between distinct nanoparticles can be regulated.

### 2.4. Rattle-type NPNS@MOF nanohybrids

Rattle-type nanohybrids with multiple nanoparticles as the cores inside a hollow shell have attracted significant attention among the complex hollow nanoarchitecture owing to their various advantages, including quicker mass transfer than that of their solid counterparts, appealing architectures, and tunable chemical and physical properties.[62–68] An early example of rattle-type NPNS@MOF nanohybrids was reported

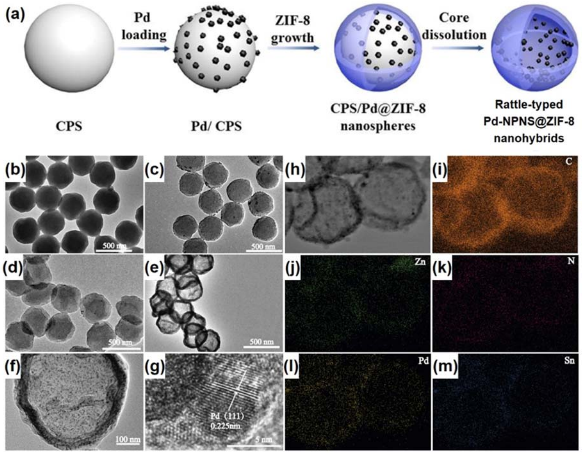

Fig. 11 (a) Schematic illustration for the preparation of rattle-type Pd-NPNS@ZIF-8 nanohybrids; (b–f) TEM images of (b) CPS, (c) Pd/CPS, (d) Pd/CPS@ZIF-8, (e and f) rattle-type Pd-NPNS@ZIF-8 nanohybrids; (g) HR-TEM images of rattle-type Pd-NPNS@ZIF-8 nanoparticles; (h–m) TEM image and elemental mapping of rattle-type Pd-NPNS@ZIF-8 nanohybrids, including (i) carbon (in orange), (j) zinc (in green), (k) nitrogen (in red), (l) palladium (in yellow), and (m) tin (in blue) (Copyright 2016, Wiley-VCH).[69]

by Wang *et al.*, in which the "ship-around-the-bottle" approach was employed through self-assembly of the Pd precursor and ZIF-8 with the help of a PS template to construct the rattle-type Pd-NPNS@MOF nanostructures (Fig. 11).[69,70] In this process, carboxylate-terminated polystyrene spheres (CPSs) were first used as the template for embedding Pd nanoparticles *via in situ* reduction with Sn(II) ions to afford CPS/Pd. Next, ZIF-8 nanocrystals were grown on the surface of CPS/Pd to generate core–shell CPS/Pd@ZIF-8 nanosystems. Finally, the CPS cores were etched with DMF to obtain the rattle-type Pd-NPNS@ZIF-8 nanoarchitectures. As shown in Fig. 11f and g, the Pd nanoparticles were well-dispersed inside the ZIF-8 shell with an average particle size of approximately 5 nm, and no free-Pd nanoparticle on the external surface of nanohybrids was observed. Moreover, one of the interesting points of this study is the use of CPS as a sacrificial polymeric support, which offers an environment to load Pd nanoparticles and can be removed by simple washing with DMF at the end of the process. The resulting rattle-type Pd-NPNS@ZIF-8 nanoparticles showed high catalytic performance for size-selective catalysis of linear alkenes in liquid-phase solutions. A similar strategy was also used to prepare the rattle-type Pd-NPNS@ZIF-8 nanoarchitecture (Fig. 12).[71] The main difference in the process compared with previous investigation[69] is the use of polyvinylpyrrolidone-stabilized polystyrene microspheres instead of carboxylate-terminated polystyrene spheres.

To extend the utilization of polystyrene spheres in the preparation of rattle-type NPNS@MOF nanohybrids, Zhong *et al.* demonstrated the hierarchical fabrication of a rattle-type $Fe_3O_4$@Pd-NPNS@ZIF-8 nanoarchitecture through a layer-by-layer synthetic procedure (Fig. 13).[72] In the process, polystyrene spheres were first functionalized using acrylic acid, and then $Fe_3O_4$/PS was obtained by integrating $Fe_3O_4$ nanoparticles onto the surface of carboxylate-terminated polystyrene spheres. Next, ZIF-8 nanocrystals were grown on $Fe_3O_4$/PS to obtain core–shell $Fe_3O_4$/PS@ZIF-8. Then, Pd nanoparticles were encapsulated into the ZIF-8 shell *via* an incipient wetness impregnation process to achieve $Fe_3O_4$/PS@Pd/ZIF-8 nanosystems. The outer ZIF-8 shell was coated onto the surface of the as-prepared core–shell $Fe_3O_4$/PS@ZIF-8 *via* the same solution self-assembly approach, generating the $Fe_3O_4$/PS@Pd/ZIF-8@ZIF-8 nanoarchitectures. Finally, the rattle-type $Fe_3O_4$@Pd-NPNS@ZIF-8 nanoarchitecture was fabricated by dissolving polystyrene templates in DMF. The layer-by-layer configurations of the obtained composites are shown in microscopy images (Fig. 14), confirming the successful synthesis of rattle-type NPNS@MOF nanosystems.[72]

Another interesting strategy to prepare rattle-type NPNS@MOF nanohybrids was investigated by Yoo *et al.* using a porous silica-assisted approach (Fig. 15).[73] In this study, to construct the rattle-type Au-NPNS@Zn-MOF nanohybrids, the Au nanoparticles were first integrated into the dendritic fibrous nanosilica (DFNS) template, which has a high surface area and porosity, generating DFNS/Au nanoparticles. Compared to previous hybrid nanostructures, the Au nanoparticles were well-dispersed within the nanospace of DFNS, increasing the number of exposed catalytic sites and the diffusion rate of both reactants and products in the resulting nanohybrids, even though the Au nanoparticles could not migrate freely. Zn-MOF

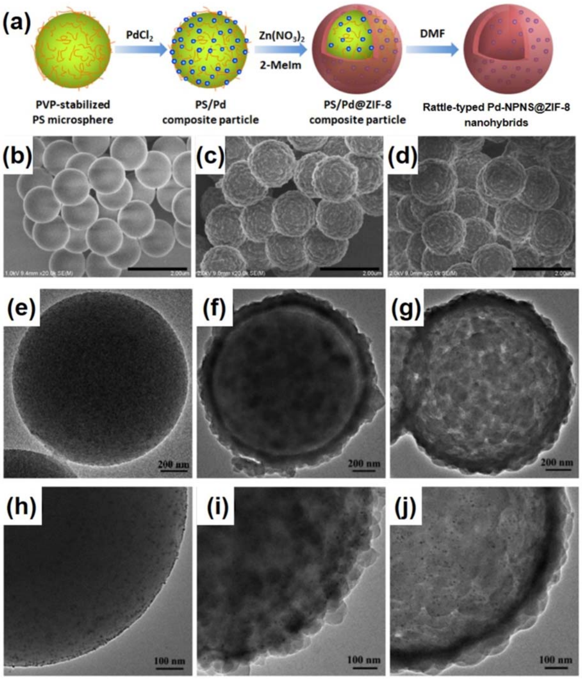

Fig. 12 (a) Schematic representation of the synthetic protocol for the preparation of rattle-type Pd-NPNS@ZIF-8 nanostructures; (b–j) SEM and TEM images of (b, e, and h) PS/Pd, (c, f, and i) core–shell PS/Pd@ZIF-8 particles, and (d, g, and j) rattle-type Pd-NPNS@ZIF-8 nanohybrids (Copyright 2020, American Chemical Society).[71]

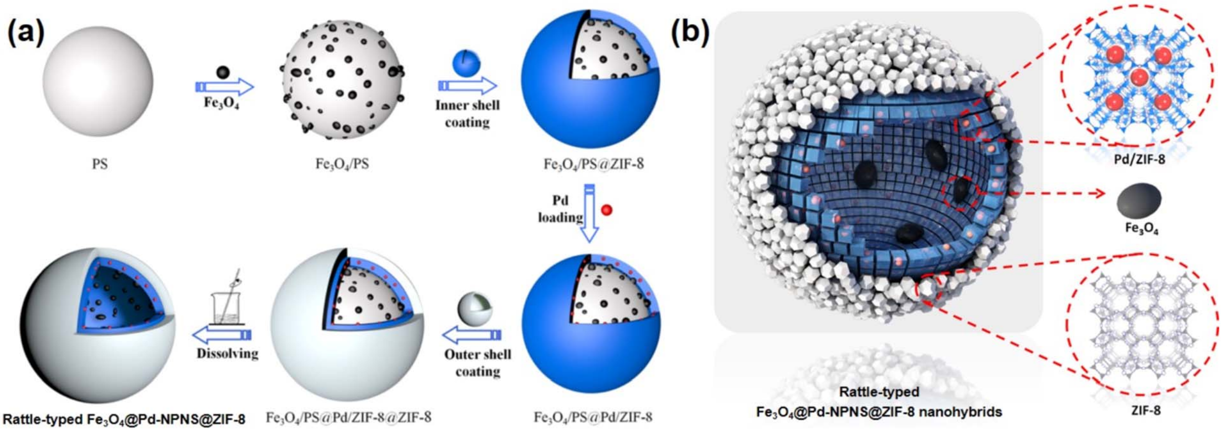

Fig. 13 (a) Schematic illustration for the fabrication and (b) structural compositions of rattle-type $Fe_3O_4$@Pd-NPNS@ZIF-8 nanoarchitectures (Copyright 2019, American Chemical Society).[72]

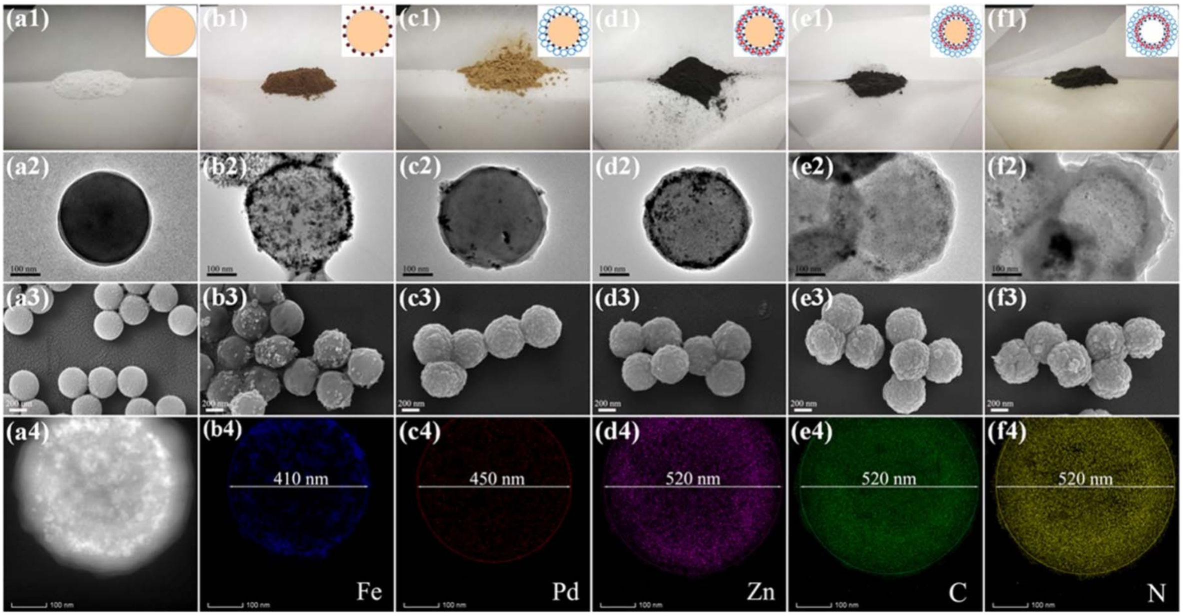

Fig. 14 Photographic images of (a1–f1, top row), TEM images (a2–f2, second row), and SEM images (a3–f3, third row) of (a) PS, (b) $Fe_3O_4$/PS, (c) $Fe_3O_4$/PS@ZIF-8, (d) $Fe_3O_4$/PS@Pd/ZIF-8, (e) $Fe_3O_4$/PS@Pd/ZIF-8@ZIF-8, and (f) rattle-type $Fe_3O_4$@Pd-NPNS@ZIF-8 nanoarchitectures, respectively; and the EDS elemental mapping data of rattle-type $Fe_3O_4$@Pd-NPNS@ZIF-8 nanoarchitectures (a4–f4, bottom row). The scale bars indicate 100 nm for TEM images and 200 nm for SEM images, respectively (Copyright 2019, American Chemical Society).[72]

nanocrystals were then grown on the surface of the DFNS/Au nanoparticles to afford rattle-type Au-NPNS@Zn-MOF nanohybrids. The obtained rattle-type Au-NPNS@Zn-MOF nanohybrids not only exhibit the well-defined and inherent structural features of the DFNS core and Zn-NMOF shells but also provide plentiful nanospaces, especially in the region between the DFNS template and Zn-NMOF for maximized incorporation of guest species without blocking the pores. In addition, to validate the feasibility of the synthesis paradigm, distinct Au nanoparticles or MOFs (*e.g.*, ZIF-8) were employed for the growth of Zn-NMOF or ZIF-8 to generate rattle-type Au-NPNS@MOF and Au-NPNS@ZIF-8 nanohybrids, respectively (Fig. 16). A novel synthetic protocol to fabricate rattle-type Ni-NPNS@MOF nanohybrids was investigated using a carboxylate-based Ni-MOF-74 shell loaded onto Ni-NPNS-loaded $SiO_2$ hollow nanospheres.[74]

## 2.5. Dot-in-shell NPNS@MOF nanohybrids

Dot-in-shell NPNS@MOF nanohybrids refer to nanoparticles dispersed within a single or multiple shells of hollow nanostructures.[75–78] In the case of multiple shells, the nanoparticles can be confined between the two shells[79] or within the first shell from the inside (Fig. 17a).[80,81] The nanospace in the structure can improve mass transfer for both reactants and

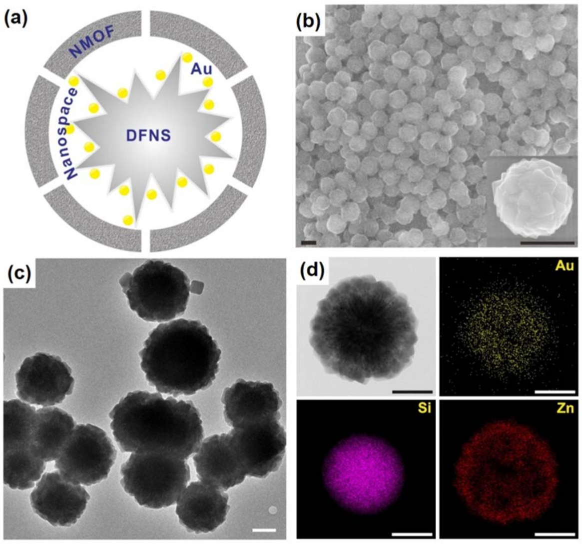

Fig. 15 (a) Structural compositions, (b) SEM images, (c) TEM image, and (d) TEM image and EDX elemental mapping data of rattle-type Au-NPNS@Zn-MOF nanohybrids, showing gold (in yellow), silica (in purple), and zinc (in red). Scale bars in (b) and (c and d) are 500 nm and 250 nm, respectively (Copyright 2020, Springer Nature).[73]

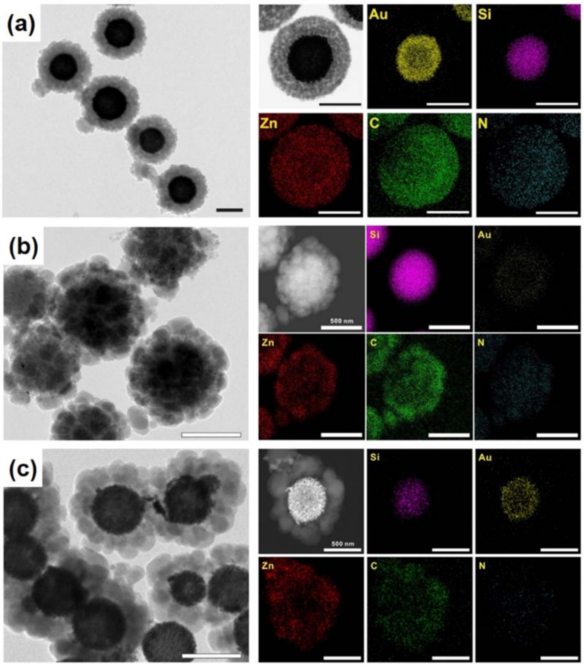

Fig. 16 TEM image and the corresponding EDX elemental mapping data for (a) rattle-type Au-NPNS@Zn-MOF nanohybrids, and (b and c) rattle-type Au-NPNS@ZIF-8 nanohybrids with different particle sizes of Au nanoparticles, showing gold (in yellow), silica (in purple), zinc (in red), carbon (in green), and nitrogen (in blue). Scale bar: 500 nm, (Copyright 2020, Springer Nature).[73]

products. The inner MOF shell was adjacent to the nanospace and acted as a scaffold for the encapsulation of nanoparticles with or without being functionalized with a capping agent.

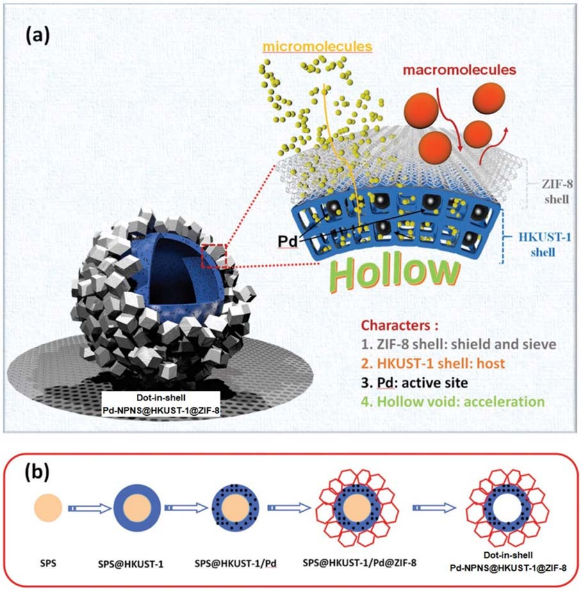

Fig. 17 (a) Schematic illustration for the compositional structure of the dot-in-shell Pd-NPNS@HKUST-1@ZIF-8 nanohybrids and (b) schematic representation for the synthetic procedure of dot-in-shell Pd-NPNS@HKUST-1@ZIF-8 nanoarchitectures (Copyright 2017, Wiley-VCH).[80]

Meanwhile, the outer MOF shell can serve not only as a protective layer but also as a size-selective sieve. An interesting example of using this strategy to prepare dot-in-shell NPNS@MOF nanohybrids was reported by Wan *et al.* (Fig. 17b),[80] in which sulfonated polystyrene spheres (SPSs) were used as the template for loading an inner HKUST-1 shell by the layer-by-layer method to generate SPS@HKUST-1. Next, Pd nanoparticles were integrated into the HKUST-1 *via* solution impregnation to yield SPS@HKUST-1/Pd. ZIF-8 was then grown on the outer surface of HKUST-1 to obtain the SPS@HKUST-1/Pd@ZIF-8 nanosystems. Finally, the SPS template was removed by dissolving to afford dot-in-shell Pd-NPNS@HKUST-1@ZIF-8 nanohybrids (Fig. 18).[80]

Liu *et al.* demonstrated a simpler strategy for preparing dot-in-shell Au-NPNS@HKUST-1 nanostructures comprising Au nanoparticles dispersed within the HKUST-1 shell (Fig. 19).[82] The synthesis protocol included the generation of Au nanoparticles on the surface of the $Cu_2O$ template, and then partially converting $Cu_2O$ to HKUST-1 to form core–shell $Cu_2O$/Au@HKUST-1 nanoparticles *via* a coordination replication reaction. Finally, residual $Cu_2O$ was removed by acid etching with acetic acid in ethanolic solution to afford dot-in-shell Au-NPNS@HKUST-1 nanohybrids. During the synthesis, the $Cu_2O$ template not only acted as a redox agent for the generation of Au nanoparticles on its surface but also converted them into a HKUST-1 nanoarchitecture through a coordination replication reaction to encapsulate the preformed Au NPs. Moreover, it is important to note that the volume ratio of ethanol to *N*,*N*-dimethylacetamide played a vital role in the growth of well-defined dot-in-shell Au-NPNS@HKUST-1 nanohybrids because

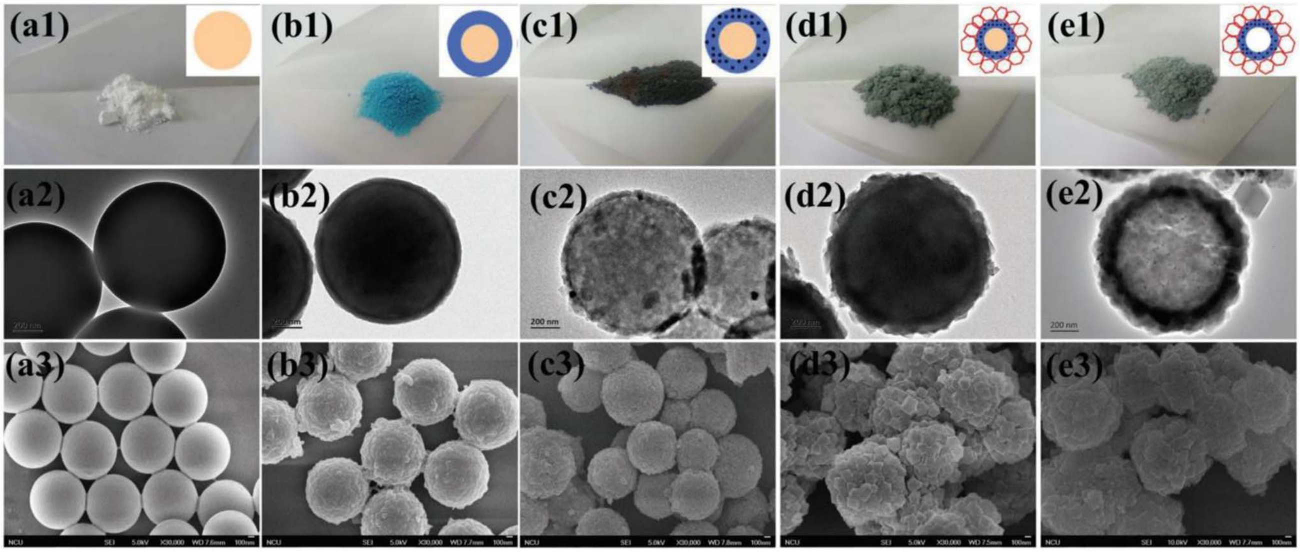

Fig. 18 The photographic (top row), TEM (middle row), and SEM (bottom row) images for (a) SPS, (b) SPS@HKUST-1, (c) SPS@HKUST-1/Pd, (d) SPS@HKUST-1/Pd@ZIF-8, and (e) Pd-NPNS@HKUST-1@ZIF-8 nanohybrids. The scale bars are 200 nm for TEM and 100 nm for SEM images, respectively (Copyright 2017, Wiley-VCH).[80]

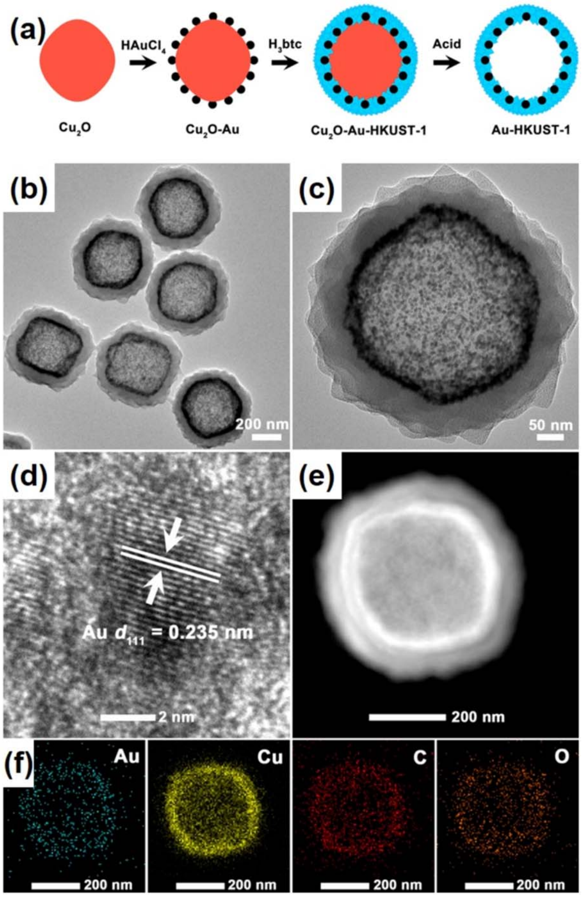

Fig. 19 (a) Schematic illustration for the preparation of dot-in-shell Au-NPNS@HKUST-1 nanostructures; (b and c) TEM images, (d) HR-TEM image, (e) HAADF-STEM image, and (f) EDX elemental mapping of the dot-in-shell Au-NPNS@HKUST-1 nanohybrids (Copyright 2016, American Chemical Society).[82]

the kinetic coupling between the coordination rate of Cu(II) ions with BTC$^{3-}$ ions and the oxidative dissolution rate of $Cu_2O$ was affected by mixed solvent use. This controllable coordination replication strategy is promising for the fabrication of other types of dot-in-shell NPNS@MOF nanohybrids.

NPNS@MOF hybrid nanomaterials, consisting of five categories including yolk–shell, multiyolk–shell, yolk–multishell, rattle-type, and dot-in-shell nanohybrids, can be prepared using various methods (Table 1). These methods include self-template or sacrificial-template methods, selective etching or dissolution–precipitation processes, bottle-around-the-shop or ship-around-the-bottle techniques, and layer-by-layer approaches. Compared to different structures, such as core–shell systems, NPNS@MOF hybrids possess a hierarchical architecture with unique features and tunable physical and chemical properties. Notably, they contain nanospace with multiple advantageous properties. In the NPNS@MOF structure, nanoparticles serve as the cores and can freely move within the nanospace. They function as active sites and are protected by the MOF shell, preventing aggregation and allowing more active sites to be exposed during processes. The outer MOF shell not only safeguards the cores but also facilitates mass transport and exchange due to its inherent high specific surface area and porosity. By adjusting the structure of the core and the shell, the diffusion rates of substrates can be controlled. The nanospace provides a homogeneous microenvironment and enhances accessibility to active sites, playing a crucial role in the improved activities of NPNS@MOF compared to other hybrid systems. However, the construction of NPNS@MOF hybrids often requires complicated and highly desirable synthesis procedures. Additionally, precise control over the morphology and composition of the inner NPNS and the outer MOF is critical for the practical applications of NPNS@MOF nanohybrids.

Table 1 Summary of the preparation of NPNS@MOF hybrid nanomaterials with various synthetic strategies and structural features

| NPNS@MOF hybrid nanomaterials | Synthesis strategies | Structural features | Applications | Ref. |
|---|---|---|---|---|
| Yolk–shell Pd-NPNS@ZIF-8 | $Cu_2O$ sacrificial template | Uniform and well-defined pore size serves as a molecular sieve | Size-selectivity hydrogenation catalysis | 47 |
| Yolk–shell hematite-NPNS@ZIF-8, yolk–shell silica-NPNS@ZIF-8 | PVP assisted-hematite or silica self-template | Yolk–shell converted from core–shell together with recrystallization of ZIF-8 | N/A | 48 |
| Yolk–shell Pd-NPNS@ZIF-8 | ZnO self-template | Molecular sieve yolk–shell converted from core–shell | Size-selectivity hydrogenation catalysis | 49 |
| Yolk–shell Au-NPNS@ZIF-8 | Etching the core–shell Au@ZIF-8 with tannic acid | Uniform and monodisperse of Au@ZIF-8 nanoparticles | Drug carrier for chemo-photothermal synergistic therapy | 54 |
| Yolk–shell $Co_3O_4$-NPNS@MOFs | Sulfate radical-based advanced-oxidation processes in the nanospace, PVP as the stabilizer | Combination of mesoporous and adsorptive bimetallic MOFs and the unique nanospace | Degradation of organic pollutants | 56 |
| Multiyolk–shell Au-NPNS@ZIF-8 | $SiO_2$ sacrificial template. PVP as the surfactant | Multiple Au yolks in a one shell ZIF-8 nanostructure | Size-selectivity aerobic oxidation of alcohols with various molecular sizes | 58 |
| Multiyolk–shell $Cu_2O$NPNS@ZIF-8 | Ultrasound-assisted $Cu_2O$ nanocube preparation, template protection–sacrifice method to encapsulate metastable $Cu_2O$ nanoparticles | $SiO_2$ served as a sacrificial template and a protective shell for $Cu_2O$ | High activity and excellent stability for the reduction of 4-nitrophenol | 59 |
| Multiyolk–shell Pd-NPNS@UiO-66-$(OH)_2$ | Oxidative linker cleaving method through oxidative ring-opening reactions, 2,5-dihydroxyterephthalic acid as a sacrificial linker | UiO-66-$(OH)_2$ shell was directionally engraved to generate the multiyolk–shell structure | Molecular-size selectivity for the conversion of cycloalkanes | 60 |
| Yolk–multishell Pd-NPNS@ZIF-8@R6G@ZIF-8 | Multi-layered ZIF nanocrystal *via* epitaxial layer-by-layer growth processes | Well-defined onion configuration, energy transfer interactions were controllably regulated | Biomimetic cascade catalysis and drug delivery | 61 |
| Rattle-type Pd-NPNS@ZIF-8 | Carboxylate-terminated polystyrene as the sacrificial template | Unprotected Pd nanoparticles dispersed in ZIF-8 hollow nanospheres | Size-selective liquid-phase hydrogenation of olefins | 69 |
| Rattle-type Pd-NPNS@ZIF-8 | PVP-stabilizer polystyrene as the sacrificial template | Pd nanoparticles encapsulated in ZIF-8 hollow nanospheres | Size-selective hydrogenation of alkenes | 71 |
| Rattle-type $Fe_3O_4$-@Pd-NPNS@ZIF-8 | Polystyrene-*co*-acrylic acid as the sacrificial template | $Fe_3O_4$ and Pd nanoparticles encapsulated within the ZIF-8 hollow sphere | Size selectivity and high reusability for styrene hydrogenation | 72 |
| Rattle-type Au-NPNS@Zn-MOF | Amine functionalized DFNS as the support | DFNS/Au nanoparticles were uniformly encapsulated within Zn-NMOF | Knoevenagel condensation reaction | 73 |
| Dot-in-shell Pd-NPNS@HKUST-1@ZIF-8 | Sulfonated-polystyrene microsphere as the sacrificial template | Inner HKUST-1 shell hosted the well dispersed Pd nanoparticles, outer ZIF-8 shell acted as the protective layer | Size-selective liquid-phase hydrogenation reaction | 80 |
| Dot-in-shell Au-NPNS@HKUST-1 | Coordination replication strategy using a $Cu_2O$ redox-template | Ethanol/DMA ratio influenced the kinetic coupling between the oxidative dissolution rate of $Cu_2O$ and coordination rate of $Cu^{2+}$ with the organic ligand | Good durability and recyclability for the CO oxidation reaction | 82 |

## 3. Applications of NPNS@MOF hybrid nanomaterials

### 3.1. Catalysis

In a given NPNS@MOF nanohybrid, the nanoparticles provide catalytically active sites for the reactants, whereas, the MOF shell acts as a barrier layer to prevent the agglomeration of the active sites with neighboring nanoparticles during the reaction. In addition, compared with the corresponding core–shell nanocatalyst, in which the shell is directly grown on the surface of nanoparticles, the nanospace generated between the nanoparticles and the MOF shell in the NPNS@MOF nanohybrids can not only serve larger exposed catalytic sites for the reactants but also lead to more homogeneous interactions between the reactants and nanoparticles. Moreover, the MOF counterpart in NPNS@MOF nanohybrids can also exhibit multiple functions in the catalytic process, such as size selectivity catalysis and regulation of mass transfer. For example, in yolk–shell Pd-NPNS@ZIF-8 nanohybrids,[47] the uniform and well-defined pore size of the ZIF-8 shell could serve as a molecular sieve for the size-selectivity hydrogenation catalysis of cyclooctene (5.5 Å), cyclohexene (4.2 Å), and ethylene (2.5 Å) (Fig. 20a). Because the pore aperture of ZIF-8 is 3.4 Å, the ZIF-8 shell could selectively allow ethylene and cyclohexane, which are smaller than the size of ZIF-8 pore aperture, to pass through and access the Pd-NPNS, while blocking cyclooctene molecules. In addition, compared to core–shell Pd@ZIF-8 nanostructures, yolk–shell Pd-NPNS@ZIF-8 nanohybrids showed different catalytic performances for cyclohexene hydrogenation with higher activation energy (40.1 kJ mol$^{-1}$), demonstrating the influence of nanospace in the yolk–shell Pd-NPNS@ZIF-8 structure. It was reasoned that the diffusion through the yolk–shell Pd-NPNS@ZIF-8 catalyst was configurational diffusion combined with Knudsen diffusion, whereas only configurational diffusion occurred in the case of the core–shell nanostructure. Another example demonstrated the critical role of the nanospace in the yolk–shell PdAg-NPNS@ZIF-8 nanocomposite in preferentially adsorbing the –$NO_2$ group rather than the –C═C group under light irradiation, which was not possible with the core–shell PdAg@ZIF-8. Interestingly, the yolk–shell PdAg-NPNS@ZIF-8 exhibited outstanding catalytic performance in the hydrogenation of nitrostyrene to vinylaniline, achieving a conversion rate of greater than 99% and a selectivity of 97.5% (Fig. 20b).[46] Similar catalytic data, including the molecular size selectively and reaction yield, were also achieved for aerobic oxidation reactions using multiyolk–shell NPNS@MOF nanocatalysts (Fig. 21).[58] The conversion of 1-butanol (2.9 × 7.1 Å), 1-hexanol (3.1 × 9.6 Å), and 3-phenylpropanol (6.3 × 11.9 Å) was 50.0%, 40.2%, and approximately 0%, respectively, indicating the excellent molecular-size selectivity of the multiyolk–shell Au-NPNS@ZIF-8 nanoreactor (Fig. 21a). Moreover, the catalytic performance of the multiyolk–shell Au-NPNS@ZIF-8 nanohybrids was higher than that of the core–shell Au@ZIF-8 nanostructures. The analysis data further confirmed the benefits of the nanospace region, which significantly facilitated the diffusion of reactants to the catalytically active sites, and offered sufficient space for the nanoparticles to be accessible to substrates. The multiyolk–shell Au-NPNS@ZIF-8 nanohybrids also exhibited good cycling stability under the investigated conditions (Fig. 21b).

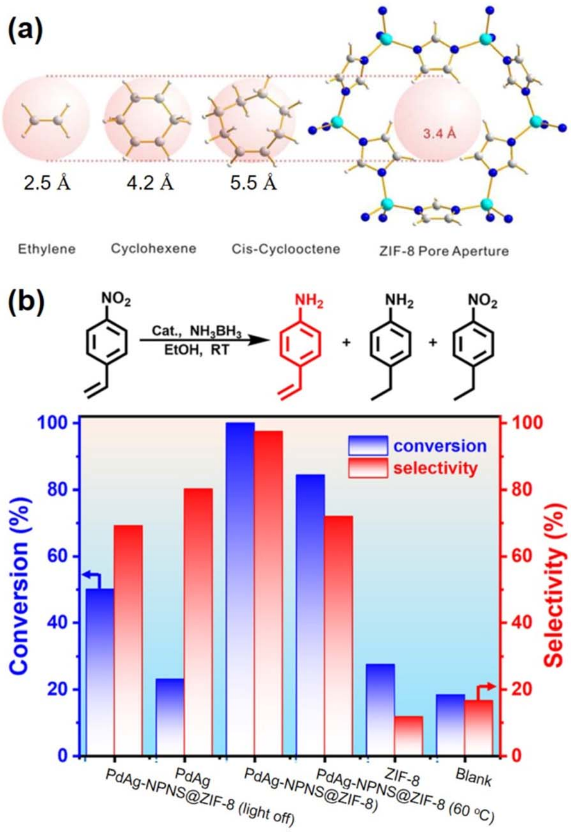

Fig. 20 (a) Molecular-size-selective catalysis of yolk–shell Pd-NPNS@MOF[47] and (b) chemoselective hydrogenation of *para*-nitrostyrene over PdAg-NPNS@ZIF-8 and different catalysts[46] (Copyright 2012 and copyright 2022, American Chemical Society).

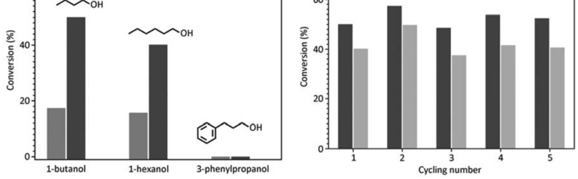

Fig. 21 Catalytic activities of multiyolk–shell Au-NPNS@ZIF-8 nanohybrids in the aerobic oxidation of alcohols: (a) conversion of 1-butanol, 1-hexanol, and 3-phenylpropanol over different catalysts and (b) catalytic stability of multiyolk–shell Au-NPNS@ZIF-8 nanohybrids (Copyright 2016, Wiley-VCH).[58]

Both the free NPNS and the immobilized NPNS showed good catalytic performance. The incorporation of the Au nanoparticles within the nanospace between the DFNS and Zn-NMOFs to yield the rattle-type Au-NPNSs@Zn-NMOF nanohybrids led to a remarkable increase in the catalytic

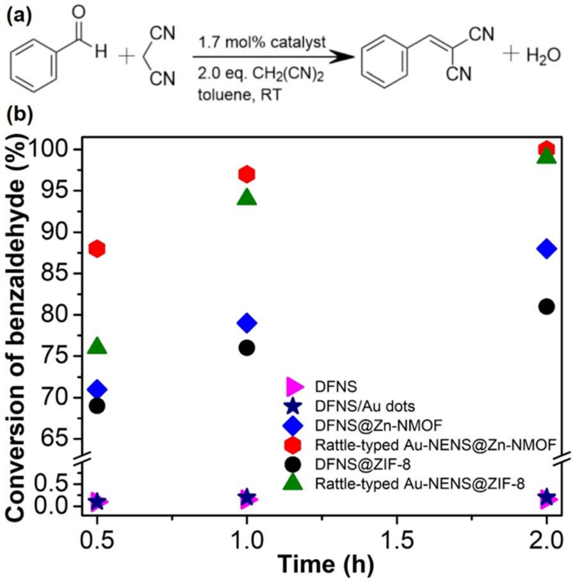

Fig. 22 (a) Knoevenagel condensation reaction scheme and (b) the conversion of benzaldehyde *versus* reaction time, using DFNS (in pink), DFNS/Au dots (in navy), DFNS@Zn-NMOF (blue), rattle-type Au-NPNS@Zn-NMOF (red), DFNS@ZIF-8 (in black), and rattle-type Au-NPNS@ZIF-8 (in dark green) as catalysts. The catalyst quantity is 1.7 mol% (Copyright 2020, Springer Nature).[73]

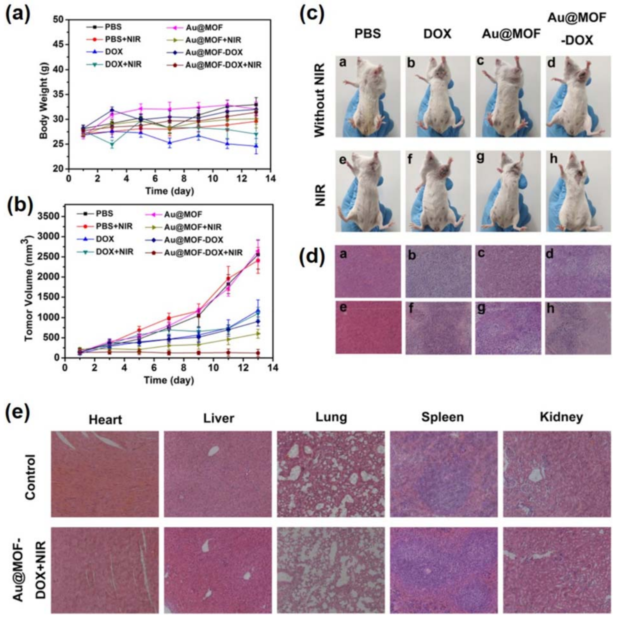

Fig. 23 *In vivo* DOX, Au@MOF, and yolk–shell Au-NPNS@ZIF-8-DOX were injected intravenously into tumor-bearing mice and treated with or without 1064 nm laser irradiation. (a) The average body weight of tumor-bearing mice in each group during the treatment periods. (b) The relative tumor volumes (normalized) of tumor-bearing mice in each group. (c) The representative photographs of tumor-bearing mice after different treatments. (d) H&E staining images of tumor sections in each group. (e) H&E stained sections of the main mice organs after treatment with PBS and yolk–shell Au-NPNS@ZIF-8-DOX with NIR irradiation (Copyright 2019, American Chemical Society).[54]

performance for the Knoevenagel condensation reaction (Fig. 22).[73] After 30 min of reaction, 88% conversion of benzaldehyde was achieved with the rattle-type Au-NPNSs@Zn-NMOF nanohybrids, which was considerably higher than those of the investigated catalysts. Moreover, compared to the rattle-type Au-NPNSs@ZIF-8 nanohybrids, the rattle-type Au-NPNSs@Zn-NMOF nanohybrids showed higher catalytic performance owing to the presence of the ligand [N3] in the structure. It was proposed that the presence of the [N3] ligand in Zn-NMOF not only increased the number of active nitrogen species but also promoted the generation of additional beneficial defects in the resulting nanocatalysts.

### 3.2. Biomedical applications

Recently, in the field of biomedical applications, NPNS@MOF nanohybrids have received increasing attention since they are suitable for integrating distinct compositional moieties and functionalities to afford an effective "all-in-one" therapeutic process. More importantly, the nanospace within the structure of NPNS@MOF nanohybrids can act as a reservoir for filling more cargo than that of core–shell nanosystems. The MOF shell not only preserves the protective function but also allows the guest species to diffuse in and out. For instance, yolk–shell Au-NPNS@ZIF-8 nanohybrids[54] were used for encapsulating doxorubicin hydrochloride (DOX), a type of chemotherapy medicine, into its nanospace to yield yolk–shell Au-NPNS@ZIF-8-DOX nanostructures. In the resulting nanosystem, Au-NPNS could be simultaneously utilized for photothermal therapy, infrared photothermal imaging, and photoacoustic imaging due to its intense NIR-II (1000–1350 nm) absorption ability, whereas the nanospace was employed for DOX delivery as a storage vessel (Fig. 23). As shown in Fig. 23a and b, the obtained data indicated that a certain inhibitory effect on the tumor was achieved through the yolk–shell NPNS@MOF-induced photothermal effect. The group treated with yolk–shell Au-NPNS@ZIF-8-DOX showed better tumor suppression activity than those treated with DOX or DOX combined with 1064 nm laser irradiation DOX, suggesting a more effective tumor enrichment effect of yolk–shell Au-NPNS@ZIF-8-DOX than free DOX. With the help of Au-NPNS@MOF-DOX nanohybrids combined with 1064 nm laser irradiation, the investigated tumor size was significantly inhibited (Fig. 23c). The tumor section results (Fig. 23d) confirmed the synergistic effect of chemotherapy and photothermal therapy over yolk–shell Au-NPNS@ZIF-8-DOX nanohybrids combined with a NIR laser. The pathomorphological data of the important visceral organs indicated that no significant apparent lesion of tissue sections was achieved in the therapeutic groups (Fig. 23e).

### 3.3. Energy-related applications

Unlike the aforementioned applications, the direct use of NPNS@MOFs for energy-related applications is still limited owing to the low electrical conductivity of MOFs.[83–85] Nevertheless, NPNS@MOF modified by post-treatments such as pyrolysis,[86–88] doping active elemental species (metal or non-metal),[89–91] and incorporating conductive materials (such as

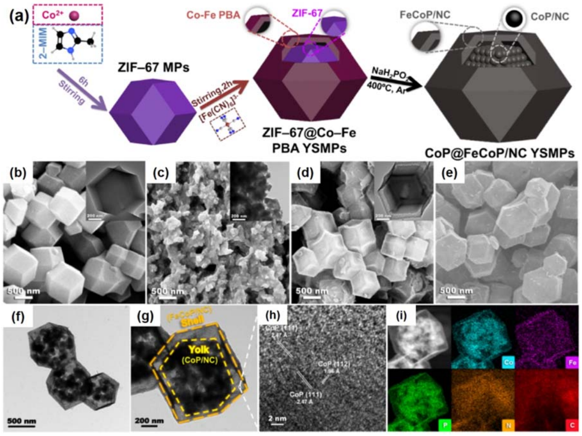

Fig. 24 (a) Schematic illustration of the formation process of CoP@FeCoP/NC YSMPs. (b–d) SEM images of (b) ZIF-67 MPs, (c) CoP/NC NPs, and (d) ZIF-67@Co–Fe PBA YSMPs. Insets of (b–d) show the corresponding TEM images. (e) SEM, (f and g) TEM and (h) HR-TEM images of CoP@FeCoP/NC YSMPs. (i) HAADF-STEM and elemental mapping images for Co, Fe, P, N, and C of CoP@FeCoP/NC YSMPs (Copyright 2021, Elsevier).[98]

graphene),[92–94] also known as NPNS@MOF-derived materials, are widely applied for energy-related applications. The NPNS@MOF-derived nanostructure obtained after post treatments not only inherits the porous templates of NPNS@MOF but also exhibits excellent electrical conductivity.[95,96] Moreover, owing to the uniquely designed structure and the interaction between the yolk and the shell, NPNS@MOF-derived materials have proven to be the most promising catalysts for energy conversion applications.[95,97] For instance, nitrogen-doped carbon-decorated CoP@FeCoP yolk-shelled micro-polyhedra (CoP@FeCoP/NC) were used as a dual-catalyst for the hydrogen evolution reaction (HER) and oxygen evolution reaction (OER) of the water splitting process (Fig. 24).[98] Their superior electrocatalytic performance stems from the interaction between the yolk CoP/NC and the shell FeCoP/NC. During the operation, FeCoP/NC prevented the aggregation of CoP/NC, and therefore, more catalytically active sites could be exposed. Furthermore, the yolk–shell structure also affects the electronic interaction of the material. In Fig. 25, FeCoP/NC and CoP/NC had excited energy band gaps of 2.26 eV and 2.05 eV, and the conductive band of −2.26 eV and −2.05 eV, respectively. Therefore, the electrons can migrate from the shell FeCoP/NC to the core CoP/NC, creating more effective electron transitions and an enormous number of active sites on CoP/NC. To confirm the superior electrocatalytic performance of the yolk–shell architecture compared with the hollow structure counterpart, Sun *et al.* investigated the OER activity of $Zn_xCo_{3-x}O_4$ yolk–shell particles ($Zn_xCo_{3-x}O_4$ YSP) and $Zn_xCo_{3-x}O_4$ hollow particles ($Zn_xCo_{3-x}O_4$ HP).[99] The obtained data indicate the stronger catalytic activity of the yolk–shell particle than the hollow counterpart (Fig. 26). The overpotential at 10 mA cm$^{-2}$ of $Zn_xCo_{3-x}O_4$ YSP was 337 mV with a Tafel slope of 59.3 mV dec$^{-1}$, while the overpotential at 10 mA cm$^{-2}$ and Tafel slope of $Zn_xCo_{3-x}O_4$ HP were higher with the corresponding values of 360 mV and 73.5 mV dec$^{-1}$ (Fig. 26a, b). For further comparison, the charge transfer resistance of $Zn_xCo_{3-x}O_4$ YSP and $Zn_xCo_{3-x}O_4$ HP was determined by electrochemical impedance spectroscopy (Fig. 26c). The $R_{ct}$ value of $Zn_xCo_{3-x}O_4$ YSP was 2.2 Ω, smaller than that of $Zn_xCo_{3-x}O_4$ HP (5.0 Ω), indicating the better electronic transportation of $Zn_xCo_{3-x}O_4$ YSP. The durability of $Zn_xCo_{3-x}O_4$ YSP was also better than that of its hollow structure counterpart with the current density nearly unchanged after 12 h of continuous operation; in the case of $Zn_xCo_{3-x}O_4$ HP, a rapid current loss of 35% was recorded (Fig. 26d). The durable activity of $Zn_xCo_{3-x}O_4$ YSP is related to its unique yolk–shell structure.

In addition, the charge interaction between the yolk and shell of the NPNS@MOF-derived material also benefits the electron transfer ability of the catalyst. Zhou *et al.* reported the synergetic effects of electrical interaction between the yolk

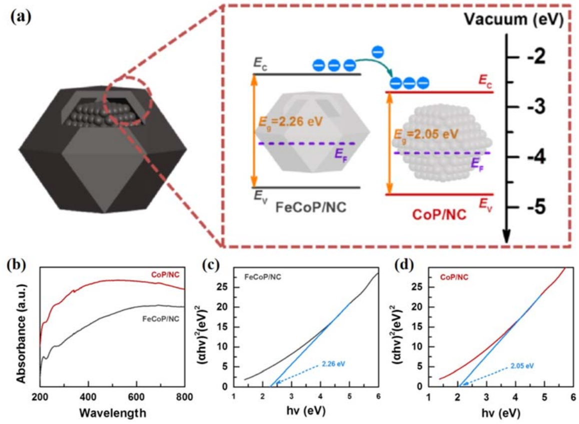

Fig. 25 (a) Schematic energy band diagram of CoP@FeCoP/NC YSMPs. (b) UV absorption spectra of FeCoP/NC HMPs and CoP/NC NPs. The Tauc–Mott plots of (c) FeCoP/NC HMPs and (d) CoP/NC NPs (Copyright 2021, Elsevier).[98]

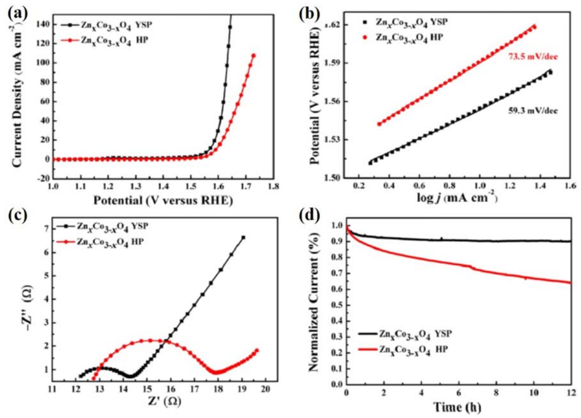

Fig. 26 (a) Linear sweep voltammetry curves and (b) Tafel plots of $Zn_xCo_{3-x}O_4$ YSP and $Zn_xCo_{3-x}O_4$ HP in an $O_2$-saturated 1 M KOH electrolyte. (c) Nyquist plots of $Zn_xCo_{3-x}O_x$ YSP and $Zn_xCo_{3-x}O_4$ HP. (d) Time-dependent current densities of $Zn_xCo_{3-x}O_4$ YSP and $Zn_xCo_{3-x}O_4$ HP (Copyright 2017, American Chemical Society).[99]

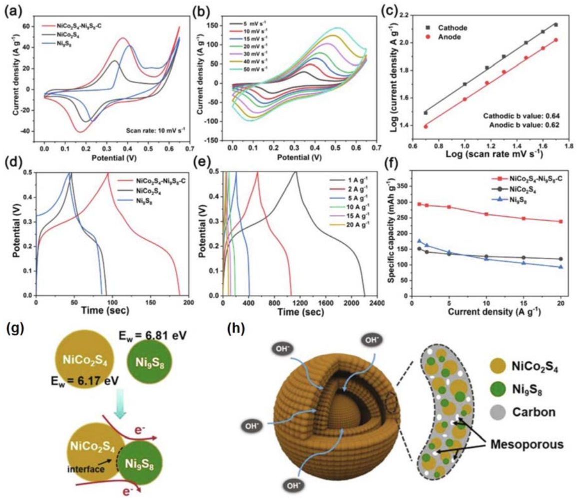

Fig. 27 (a) Cyclic voltammetry (CV) curves of the $NiCo_2S_4$–$Ni_9S_8$–C DYM electrode at different scan rates, (b) CV curves of $NiCo_2S_4$–$Ni_9S_8$–C DYM, $NiCo_2S_4$ and $Ni_9S_8$ electrodes at a scan rate of 10 mV $s^{-1}$, (c) the log *I versus* log *v* at cathodic and anodic peak current densities of the $NiCo_2S_4$–$Ni_9S_8$–C DYM electrode, (d) galvanostatic charge–discharge (GCD) curves of the $NiCo_2S_4$–$Ni_9S_8$–C DYM electrode at various current densities, (e) GCD curves of $NiCo_2S_4$–$Ni_9S_8$–C DYM, $NiCo_2S_4$ and $Ni_9S_8$ electrodes at a current density of 10 mV $s^{-1}$, (f) specific capacities of the $NiCo_2S_4$–$Ni_9S_8$–C DYM electrode at different current densities, (g) illustration of electron transfer at heterointerfaces within one $NiCo_2S_4$–$Ni_9S_8$ NP, and (h) schematic illustration of the structural advantages of the $NiCo_2S_4$–$Ni_9S_8$–C DYM electrode (Copyright 2020, Elsevier).[100]

$NiCo_2S_4$ and the shell $Ni_9S_8$ on the charge capacity of $NiCo_2S_4$–$Ni_9S_8$–C double-layer yolk–shell microspheres ($NiCo_2S_4$–$Ni_9S_8$–C DYMs) derived from bimetallic Co/Ni-MOF.[100] The $NiCo_2S_4$–$Ni_9S_8$–C DYMs exhibited a high specific capacity of 293.6 mA h $g^{-1}$ at 1.0 A $g^{-1}$, and excellent rate capacity with a value of 81.1% from 1.0 A $g^{-1}$ to 20 A $g^{-1}$ (Fig. 27a–f). For a deeper understanding, the work functions ($E_w$) and Fermi level were used to estimate the charge carrier transport ability in the materials ($E_f$) and the vacuum layer levels of $NiCo_2S_9$ and $Ni_9S_8$ were determined. By using density functional theory calculation, the $E_w$ value of the yolk $NiCo_2S_9$ and the shell $Ni_9S_8$ was 6.17 eV and 6.81 eV, and therefore, the free electron could flow from $NiCo_2S_9$ to $Ni_9S_8$ through the interfaces to balance the $E_f$ (Fig. 27g). The charge interaction generated at the interface between $NiCo_2S_9$ and $Ni_9S_8$ can improve charge diffusion and electron transfer during the charge/discharge process (Fig. 27h).

## 4. Conclusion and outlook

Significant progress has been made in the design and development of NPNS@MOF hybrid nanomaterials composed of nanoparticles, MOFs, and nanospace within their architectures over the past few decades. NPNS@MOF exhibits excellent intrinsic properties, including desired compositions, distinct morphologies, and unique structural characteristics, setting them apart from other hybrid structures. These advantageous features make them highly promising for a wide range of applications. This review provides a comprehensive description of the main synthetic strategies used to produce NPNS@MOF hybrids, such as yolk–shell, multiyolk–shell, yolk–multishell, rattle-type, and dot-in-shell nanohybrids. Additionally, the structure–property–activity relationship within the NPNS@MOF architectures is thoroughly summarized. For example, the regulation of the microenvironment surrounding catalytically active sites in the yolk–shell PdAg-NPNS@MOF results in excellent selectivity and recyclability for the hydrogenation of nitrostyrene. Importantly, the synergistic effect of the exceptional structural advantages offered by nanoparticles as cores and MOFs as shells, along with the nanospace generated within the structure, significantly enhances the performance of NPNS@MOF in targeted processes, including activity, durability, and recyclability. In this context, the nanospace enables (i) greater accessibility to exposed catalytically active sites, (ii) regulation of the microenvironment and interactions of active species, (iii) sufficient space for mass and/or charge transfer, and (iv) stabilization of active species to prevent agglomeration.

Despite the aforementioned achievements in this field, the development of NPNS@MOF hybrid nanomaterials is still in its infancy. The design and regulation face plentiful obstacles, especially, their applicability is far from practical requirements. (1) The main drawback is the weak stability of MOFs in terms of chemical and thermal characteristics, resulting from the inherent coordination bonding and organic components. Additionally, the current reported MOFs' pore size and/or aperture are suitable for size-selective reagents, but there is a high demand for size selectivity in targeted product formation in technological processes. (2) The growth of nanoparticles in terms of size, shape, and composition within NPNS@MOF is still uncertain. The arrangement of nanoparticles within the MOF shell is currently limited to random placement. Moreover, the interaction of nanoparticles with the MOF substrate lacks detailed structural information, thereby impacting the understanding of the structure–activity relationship. (3) Complicated and expensive synthesis procedures, as well as issues of scalability and universality, pose additional barriers to the practical utilization of NPNS@MOF.

As NPNS@MOF research progresses, attention has gradually shifted from synthesis, including morphology, structure, and activity measurements, to the demonstration of multifunctional properties and capabilities in industrial applications. However, challenges persist due to the aforementioned drawbacks, necessitating significant efforts for further development in this area. This review aims to provide a comprehensive understanding and insightful perspectives on NPNS@MOF hybrid nanomaterials by offering detailed information on their synthetic methods, structures, and corresponding applications, and ultimately facilitate the design and development of novel NPNS@MOF materials for future use.

## Conflicts of interest

There are no conflicts to declare.

## Acknowledgements

This work was supported by the Korea Institute for Advancement of Technology (KIAT) grant funded by the Korea Government (Ministry of Trade, Industry and Energy, MOTIE) (P0008425, The Competency Development Program for Industry Specialist). This work was also supported by the National Research Foundation of Korea (NRF) grant funded by the Korea government (Ministry of Science and ICT, MSIT) (the Bio & Medical Technology Development Program (No. RS-2023-00223501) and NRF-2020R1A2C1004006).

## References

1 L. Chen and Q. Xu, *Matter*, 2019, **1**, 57–89.
2 Q. Wang and D. Astruc, *Chem. Rev.*, 2020, **120**, 1438–1511.
3 Q.-L. Zhu and Q. Xu, *Chem. Soc. Rev.*, 2014, **43**, 5468–5512.
4 X. Cai, Z. Xie, D. Li, M. Kassymova, S.-Q. Zang and H.-L. Jiang, *Coord. Chem. Rev.*, 2020, **417**, 213366.
5 H. Furukawa, K. E. Cordova, M. O'Keeffe and O. M. Yaghi, *Science*, 2013, **341**, 1230444.
6 H.-L. Jiang and Q. Xu, *Chem. Commun.*, 2011, **47**, 3351–3370.
7 T. A. Goetjen, J. Liu, Y. Wu, J. Sui, X. Zhang, J. T. Hupp and O. K. Farha, *Chem. Commun.*, 2020, **56**, 10409–10418.
8 R. Freund, O. Zaremba, G. Arnauts, R. Ameloot, G. Skorupskii, M. Dincă, A. Bavykina, J. Gascon, A. Ejsmont, J. Goscianska, M. Kalmutzki, U. Lächelt, E. Ploetz, C. S. Diercks and S. Wuttke, *Angew. Chem., Int. Ed.*, 2021, **60**, 23975–24001.
9 Y.-N. Gong, L. Jiao, Y. Qian, C.-Y. Pan, L. Zheng, X. Cai, B. Liu, S.-H. Yu and H.-L. Jiang, *Angew. Chem., Int. Ed.*, 2020, **59**, 2705–2709.
10 T. Islamoglu, S. Goswami, Z. Li, A. J. Howarth, O. K. Farha and J. T. Hupp, *Acc. Chem. Res.*, 2017, **50**, 805–813.
11 W. Lu, Z. Wei, Z.-Y. Gu, T.-F. Liu, J. Park, J. Park, J. Tian, M. Zhang, Q. Zhang, T. Gentle III, M. Bosch and H.-C. Zhou, *Chem. Soc. Rev.*, 2014, **43**, 5561–5593.
12 J. Lee, O. K. Farha, J. Roberts, K. A. Scheidt, S. T. Nguyen and J. T. Hupp, *Chem. Soc. Rev.*, 2009, **38**, 1450–1459.
13 Q.-L. Zhu, W. Xia, T. Akita, R. Zou and Q. Xu, *Adv. Mater.*, 2016, **28**, 6391–6398.
14 R. E. Morris and L. Brammer, *Chem. Soc. Rev.*, 2017, **46**, 5444–5462.
15 H. Xu, H. Shang, C. Wang, L. Jin, C. Chen, C. Wang and Y. Du, *Appl. Catal., B*, 2020, **265**, 118605.
16 L. Li, Z. Li, W. Yang, Y. Huang, G. Huang, Q. Guan, Y. Dong, J. Lu, S.-H. Yu and H.-L. Jiang, *Chem*, 2021, **7**, 686–698.
17 B. Li, J.-G. Ma and P. Cheng, *Small*, 2019, **15**, 1804849.
18 C.-D. Wu and M. Zhao, *Adv. Mater.*, 2017, **29**, 1605446.
19 G. Cai, M. Ding, Q. Wu and H.-L. Jiang, *Natl. Sci. Rev.*, 2020, **7**, 37–45.
20 L. Jiao, J. Wang and H.-L. Jiang, *Acc. Mater. Res.*, 2021, **2**, 327–339.
21 R. Ghosh Chaudhuri and S. Paria, *Chem. Rev.*, 2012, **112**, 2373–2433.
22 H.-F. Wang, L. Chen, H. Pang, S. Kaskel and Q. Xu, *Chem. Soc. Rev.*, 2020, **49**, 1414–1448.
23 A. L. M. Reddy, S. R. Gowda, M. M. Shaijumon and P. M. Ajayan, *Adv. Mater.*, 2012, **24**, 5045–5064.
24 Y. Liu, Z. Liu, D. Huang, M. Cheng, G. Zeng, C. Lai, C. Zhang, C. Zhou, W. Wang, D. Jiang, H. Wang and B. Shao, *Coord. Chem. Rev.*, 2019, **388**, 63–78.
25 Y. Shan, L. Chen, H. Pang and Q. Xu, *Small Struct.*, 2021, **2**, 2000078.
26 F.-X. Xiao, J. Miao, H. B. Tao, S.-F. Hung, H.-Y. Wang, H. B. Yang, J. Chen, R. Chen and B. Liu, *Small*, 2015, **11**, 2115–2131.
27 L. Chen, R. Luque and Y. Li, *Chem. Soc. Rev.*, 2017, **46**, 4614–4630.
28 E. Antolini, *Appl. Catal., B*, 2016, **181**, 298–313.
29 Z. Zhao, X. Wang, X. Jing, Y. Zhao, K. Lan, W. Zhang, L. Duan, D. Guo, C. Wang, L. Peng, X. Zhang, Z. An, W. Li, Z. Nie, C. Fan and D. Zhao, *Adv. Mater.*, 2021, **33**, 2100820.
30 G. Li, S. Zhao, Y. Zhang and Z. Tang, *Adv. Mater.*, 2018, **30**, 1800702.
31 S. Subudhi, S. P. Tripathy and K. Parida, *Inorg. Chem. Front.*, 2021, **8**, 1619–1636.
32 C. S. L. Koh, H. Y. F. Sim, S. X. Leong, S. K. Boong, C. Chong and X. Y. Ling, *ACS Mater. Lett.*, 2021, **3**, 557–573.
33 Y. Liang, E. Li, K. Wang, Z.-J. Guan, H.-h. He, L. Zhang, H.-C. Zhou, F. Huang and Y. Fang, *Chem. Soc. Rev.*, 2022, **51**, 8378–8405.
34 L.-W. Chen, Y.-C. Hao, Y. Guo, Q. Zhang, J. Li, W.-Y. Gao, L. Ren, X. Su, L. Hu, N. Zhang, S. Li, X. Feng, L. Gu, Y.-W. Zhang, A.-X. Yin and B. Wang, *J. Am. Chem. Soc.*, 2021, **143**, 5727–5736.
35 A. Bavykina, N. Kolobov, I. S. Khan, J. A. Bau, A. Ramirez and J. Gascon, *Chem. Rev.*, 2020, **120**, 8468–8535.
36 T. Qiu, S. Gao, Z. Liang, D.-G. Wang, H. Tabassum, R. Zhong and R. Zou, *Angew. Chem., Int. Ed.*, 2021, **60**, 17314–17336.
37 G. Prieto, H. Tüysüz, N. Duyckaerts, J. Knossalla, G.-H. Wang and F. Schüth, *Chem. Rev.*, 2016, **116**, 14056–14119.
38 B. Li and H. C. Zeng, *Adv. Mater.*, 2019, **31**, 1801104.
39 Z.-X. Cai, Z.-L. Wang, J. Kim and Y. Yamauchi, *Adv. Mater.*, 2019, **31**, 1804903.
40 C. Gao, F. Lyu and Y. Yin, *Chem. Rev.*, 2021, **121**, 834–881.
41 Q. Yang, Q. Xu and H.-L. Jiang, *Chem. Soc. Rev.*, 2017, **46**, 4774–4808.
42 H. Yang and X. Wang, *Adv. Mater.*, 2019, **31**, 1800743.
43 B. Cui and G. Fu, *Nanoscale*, 2022, **14**, 1679–1699.
44 Y. Qian, F. Zhang, S. Zhao, C. Bian, H. Mao, D. J. Kang and H. Pang, *Nano Energy*, 2023, **111**, 108415.
45 J.-D. Xiao, R. Li and H.-L. Jiang, *Small Methods*, 2023, **7**, 2201258.
46 L. Li, Y. Li, L. Jiao, X. Liu, Z. Ma, Y.-J. Zeng, X. Zheng and H.-L. Jiang, *J. Am. Chem. Soc.*, 2022, **144**, 17075–17085.
47 C.-H. Kuo, Y. Tang, L.-Y. Chou, B. T. Sneed, C. N. Brodsky, Z. Zhao and C.-K. Tsung, *J. Am. Chem. Soc.*, 2012, **134**, 14345–14348.
48 M. Sindoro and S. Granick, *J. Am. Chem. Soc.*, 2014, **136**, 13471–13473.

49 F.-L. Li, H.-X. Li and J.-P. Lang, *CrystEngComm*, 2016, **18**, 1760–1767.

50 Y. Yang, F. Wang, Q. Yang, Y. Hu, H. Yan, Y.-Z. Chen, H. Liu, G. Zhang, J. Lu, H.-L. Jiang and H. Xu, *ACS Appl. Mater. Interfaces*, 2014, **6**, 18163–18171.

51 Y. Liu, W. Zhang, S. Li, C. Cui, J. Wu, H. Chen and F. Huo, *Chem. Mater.*, 2014, **26**, 1119–1125.

52 Z. Zhang, Y. Chen, X. Xu, J. Zhang, G. Xiang, W. He and X. Wang, *Angew. Chem., Int. Ed.*, 2014, **53**, 429–433.

53 S. Zhang, Y. Fan, L. Luo, C. Li, Y. Ma and T. Li, *Chem. Commun.*, 2021, **57**, 3415–3418.

54 X. Deng, S. Liang, X. Cai, S. Huang, Z. Cheng, Y. Shi, M. Pang, P. a. Ma and J. Lin, *Nano Lett.*, 2019, **19**, 6772–6780.

55 T. Song, F. Gao, S. Guo, Y. Zhang, S. Li, H. You and Y. Du, *Nanoscale*, 2021, **13**, 3895–3910.

56 T. Zeng, X. Zhang, S. Wang, H. Niu and Y. Cai, *Environ. Sci. Technol.*, 2015, **49**, 2350–2357.

57 Y. Xue, S. Zheng, H. Xue and H. Pang, *J. Mater. Chem. A*, 2019, **7**, 7301–7327.

58 S. Wang, Y. Fan, J. Teng, Y.-Z. Fan, J.-J. Jiang, H.-P. Wang, H. Grützmacher, D. Wang and C.-Y. Su, *Small*, 2016, **12**, 5702–5709.

59 B. Li, J.-G. Ma and P. Cheng, *Angew. Chem., Int. Ed.*, 2018, **57**, 6834–6837.

60 L. Luo, W.-S. Lo, X. Si, H. Li, Y. Wu, Y. An, Q. Zhu, L.-Y. Chou, T. Li and C.-K. Tsung, *J. Am. Chem. Soc.*, 2019, **141**, 20365–20370.

61 X.-Y. Liu, F. Zhang, T.-W. Goh, Y. Li, Y.-C. Shao, L. Luo, W. Huang, Y.-T. Long, L.-Y. Chou and C.-K. Tsung, *Angew. Chem., Int. Ed.*, 2018, **57**, 2110–2114.

62 J. Liu, S. Z. Qiao, J. S. Chen, X. W. Lou, X. Xing and G. Q. Lu, *Chem. Commun.*, 2011, **47**, 12578–12591.

63 L. Lin, H. Liu and X. Zhang, *Chem. Eng. J.*, 2017, **328**, 124–132.

64 N. Qin, A. Pan, J. Yuan, F. Ke, X. Wu, J. Zhu, J. Liu and J. Zhu, *ACS Appl. Mater. Interfaces*, 2021, **13**, 12463–12471.

65 S. Shi, Y. Yu, B. Zhang, Y. Zhong, L. Wang, S. Wang, S. Ding and C. Chen, *Front. Chem.*, 2021, **9**, 738736.

66 N. Qin, X. Wu, X. Liu, Z.-H. Xue, M. Muddassir, H. Sakiyama, C. Xia, C. Zhang, L. Zhu and F. Ke, *ACS Sustainable Chem. Eng.*, 2022, **10**, 5396–5403.

67 C. Wu, X. Zhao, D. Wang, X. Si and T. Li, *Chem. Sci.*, 2022, **13**, 13338–13346.

68 S. Shi, Y. Zhong, Z. Hu, L. Wang, M. Yuan, S. Ding, S. Wang and C. Chen, *Inorg. Chem.*, 2021, **60**, 12714–12718.

69 X. Wang, M. Li, C. Cao, C. Liu, J. Liu, Y. Zhu, S. Zhang and W. Song, *ChemCatChem*, 2016, **8**, 3224–3228.

70 A. Zanon and F. Verpoort, *Coord. Chem. Rev.*, 2017, **353**, 201–222.

71 Y. Zhao, X. Ni, S. Ye, Z.-G. Gu, Y. Li and T. Ngai, *Langmuir*, 2020, **36**, 2037–2043.

72 Y. Zhong, Y. Mao, S. Shi, M. Wan, C. Ma, S. Wang, C. Chen, D. Zhao and N. Zhang, *ACS Appl. Mater. Interfaces*, 2019, **11**, 32251–32260.

73 N. M. Tran, S. Jung and H. Yoo, *Nano Res.*, 2020, **13**, 775–784.

74 B. Li and H. C. Zeng, *Chem. Mater.*, 2019, **31**, 5320–5330.

75 B. Sun and H. C. Zeng, *Part. Part. Syst. Charact.*, 2020, **37**, 2000101.

76 H. Niu, Y. Zheng, S. Wang, L. Zhao, S. Yang and Y. Cai, *J. Hazard. Mater.*, 2018, **346**, 174–183.

77 S. Choi and M. Oh, *Angew. Chem., Int. Ed.*, 2019, **58**, 866–871.

78 J. Zhu, H. Chen, L. Wang, E. Fu, J. Wu, Q. Zhang, L. Yang and G. Xu, *Microporous Mesoporous Mater.*, 2022, **329**, 111490.

79 X. Wang, Y. Hou, X. Wang, Y. Guo and X. Zhang, *Appl. Surf. Sci.*, 2023, **608**, 155123.

80 M. Wan, X. Zhang, M. Li, B. Chen, J. Yin, H. Jin, L. Lin, C. Chen and N. Zhang, *Small*, 2017, **13**, 1701395.

81 B. Zhang, M. Li, H. Lei, J. Chen, S. Wang and C. Chen, *Appl. Surf. Sci.*, 2022, **599**, 153899.

82 Y. Liu, J. Zhang, L. Song, W. Xu, Z. Guo, X. Yang, X. Wu and X. Chen, *ACS Appl. Mater. Interfaces*, 2016, **8**, 22745–22750.

83 X. F. Lu, B. Y. Xia, S.-Q. Zang and X. W. Lou, *Angew. Chem., Int. Ed.*, 2020, **59**, 4634–4650.

84 R. Zhu, J. Ding, Y. Xu, J. Yang, Q. Xu and H. Pang, *Small*, 2018, **14**, 1803576.

85 Y. Wang, B. Liu, X. Shen, H. Arandiyan, T. Zhao, Y. Li, M. Garbrecht, Z. Su, L. Han, A. Tricoli and C. Zhao, *Adv. Energy Mater.*, 2021, **11**, 2003759.

86 T. Huang, Y. Chen and J.-M. Lee, *Small*, 2017, **13**, 1702753.

87 X. Liu, Y. Liu and L.-Z. Fan, *J. Mater. Chem. A*, 2017, **5**, 15310–15314.

88 T. Wang, X. Cao and L. Jiao, *Small*, 2021, **17**, 2004398.

89 Y.-Z. Chen, C. Wang, Z.-Y. Wu, Y. Xiong, Q. Xu, S.-H. Yu and H.-L. Jiang, *Adv. Mater.*, 2015, **27**, 5010–5016.

90 H. He, Q.-Q. Zhu, Y. Yan, H.-W. Zhang, Z.-Y. Han, H. Sun, J. Chen, C.-P. Li, Z. Zhang and M. Du, *Appl. Catal., B*, 2022, **302**, 120840.

91 Y. He, S. Yang, Y. Fu, F. Wang, J. Ma, G. Wang, G. Chen, M. Wang, R. Dong, P. Zhang and X. Feng, *Small Struct.*, 2021, **2**, 2000095.

92 P. Pachfule, D. Shinde, M. Majumder and Q. Xu, *Nat. Chem.*, 2016, **8**, 718–724.

93 H. Tang, H. Yin, J. Wang, N. Yang, D. Wang and Z. Tang, *Angew. Chem., Int. Ed.*, 2013, **52**, 5585–5589.

94 H. Saini, N. Srinivasan, V. Šedajová, M. Majumder, D. P. Dubal, M. Otyepka, R. Zbořil, N. Kurra, R. A. Fischer and K. Jayaramulu, *ACS Nano*, 2021, **15**, 18742–18776.

95 X. Cao, C. Tan, M. Sindoro and H. Zhang, *Chem. Soc. Rev.*, 2017, **46**, 2660–2677.

96 S.-H. Chae, A. Muthurasu, T. Kim, J. S. Kim, M.-S. Khil, M. Lee, H. Kim, J. Y. Lee and H. Y. Kim, *Appl. Catal., B*, 2021, **293**, 120209.

97 A. Radwan, H. Jin, D. He and S. Mu, *Nano-Micro Lett.*, 2021, **13**, 132.

98 J. Shi, F. Qiu, W. Yuan, M. Guo and Z.-H. Lu, *Chem. Eng. J.*, 2021, **403**, 126312.

99 Z. Yu, Y. Bai, Y. Liu, S. Zhang, D. Chen, N. Zhang and K. Sun, *ACS Appl. Mater. Interfaces*, 2017, **9**, 31777–31785.

100 Y. Yan, A. Li, C. Lu, T. Zhai, S. Lu, W. Li and W. Zhou, *Chem. Eng. J.*, 2020, **396**, 125316.